GW Detectors Principia

Extended Lecture Notes

STGWD 2026 — PhD International School on
Technologies in Gravitational Waves Detection

Gianluca Gemme
INFN Sezione di Genova
Virgo and ET Collaborations
gianluca.gemme@ge.infn.it

May 2026

Contents

Preface **5**

1 Block 1 — Interaction of GWs with Test Masses **7**
Block overview . . . 7
1.1 Setting the stage — why the gauge question matters . . . 7
1.1.1 Gauge freedom: physics invariant, description is not . . . 8
1.1.2 Recap — the TT gauge . . . 8
1.1.3 Recap — the Riemann tensor of a linear GW . . . 9
1.1.4 Recap — geodesic and geodesic-deviation equations . . . 9
1.1.5 Roadmap: two complementary pictures . . . 10
1.2 The TT-frame picture . . . 11
1.2.1 Test mass at rest in the TT frame . . . 11
1.2.2 Physical meaning: coordinates stretch with the wave . . . 11
1.2.3 Proper distance between free test masses . . . 12
1.2.4 Effect on a ring of test masses: plus polarization . . . 12
1.2.5 Effect on a ring of test masses: cross polarization . . . 12
1.2.6 Light propagation along one arm: setup . . . 13
1.2.7 Round-trip time: the sinc factor . . . 13
1.2.8 Regimes of the sinc factor . . . 14
1.2.9 Audio sidebands at the output . . . 15
1.3 The proper detector frame picture . . . 15
1.3.1 Why experimentalists use a different frame . . . 16
1.3.2 Fermi normal coordinates: free-falling lab . . . 16
1.3.3 Earth-bound lab: adding acceleration and rotation . . . 16
1.3.4 Hierarchy of corrections in r/L_B . . . 17
1.3.5 The Newtonian-force picture . . . 17
1.3.6 Ring of test masses: revisited in the force picture . . . 18
1.3.7 Validity and limits of the two pictures . . . 18
1.4 From test masses to detector output . . . 18
1.4.1 L-shaped detector: differential response . . . 19
1.4.2 Strain: the dimensionless observable . . . 19
1.4.3 Detector tensor and antenna pattern functions . . . 20
1.4.4 The fundamental detector output . . . 20
1.4.5 Geometry: orientation, sky location, polarization . . . 21
1.4.6 Bridge to Block 2 . . . 21
Block 1 — Summary . . . 22
Block 1 — Key equations . . . 22
Block 1 — Further reading . . . 22
Block 1 — Exercises . . . 23

2 Block 2 — Experimental Fundamentals **25**
Block overview . . . 25
2.1 From theory to instrument . . . 25
2.1.1 Recap from Block 1 and the core question . . . 26
2.1.2 The scale of the problem . . . 26
2.1.3 Why interferometry, why differential . . . 26
2.1.4 Michelson topology and dark-fringe operation . . . 27

2.1.5 The output field in the presence of a GW . . . 28
2.1.6 From phase to strain, and the sinc factor . . . 28
2.1.7 Shot-noise-limited Michelson: the benchmark number . . . 29
2.2 Why real detectors are not plain Michelsons . . . 29
2.2.1 Two handles: longer effective path, more photons . . . 30
2.2.2 Fabry–Perot arm cavities . . . 30
2.2.3 Power recycling . . . 31
2.2.4 Signal recycling . . . 31
2.2.5 Squeezing . . . 32
2.3 Noise budget — the fundamentals . . . 32
2.3.1 Two design principles . . . 32
2.3.2 The sensitivity curve as a map of the detector . . . 33
2.3.3 Seismic noise . . . 33
2.3.4 Seismic isolation . . . 33
2.3.5 Newtonian (gravity-gradient) noise . . . 34
2.3.6 Thermal noise — the fluctuation–dissipation theorem . . . 34
2.3.7 Suspension thermal noise . . . 35
2.3.8 Coating thermal noise . . . 35
2.3.9 Quantum noise: shot and radiation pressure . . . 36
2.3.10 The Standard Quantum Limit . . . 37
2.3.11 Technical noises . . . 37
2.3.12 Reading a real sensitivity curve . . . 38
2.4 Network, reach, and what comes next . . . 39
2.4.1 From strain sensitivity to astrophysical reach . . . 39
2.4.2 Why a network . . . 39
2.4.3 Sky localisation and triangulation . . . 40
2.4.4 The global network today and in the near future . . . 40
2.4.5 Third-generation detectors . . . 40
2.4.6 Bridge to the rest of the school . . . 41
Block 2 — Summary . . . 41
Block 2 — Key equations . . . 42
Block 2 — Further reading . . . 42
Block 2 — Exercises . . . 43

Preface

Prerequisites. These notes, and the lectures they accompany, assume the student is already familiar with the principles of General Relativity at the undergraduate physics level. Specifically: tensor calculus on curved manifolds, the Christoffel connection, the Riemann tensor and its symmetries, the geodesic and geodesic-deviation equations, and the linearised Einstein equations in the Lorenz gauge. A first encounter with the transverse-traceless gauge is also expected, though the relevant results are recapped in Section 1.1. Any standard textbook (Carroll, Hartle, Schutz, Wald, Weinberg, Maggiore) provides enough background.

These notes accompany the course *GW Detectors Principia*, delivered at the STGWD 2026 PhD International School on Technologies in Gravitational Waves Detection. The course consists of two lecture blocks of two hours each.

Block 1 covers how a gravitational wave interacts with a system of free test masses: the theoretical picture that sits behind the simple statement that "the detector measures a strain $h(t)$". Block 2 covers the instrument that reads $h(t)$ out of the noise: the Michelson and its descendants, the main fundamental noises, and what it takes to turn a fractional length change of order 10^{-21} into a measurable optical signal.

The expected background is General Relativity at the weak-field, linearised level: Christoffel symbols, geodesic equation, geodesic deviation, and a first encounter with the transverse-traceless (TT) gauge. Students who have not met these before should consult the references at the end of each block before starting the notes.

How to use the notes. The slide deck carries the essential equations and diagrams. These notes fill in the steps that there is no time to cover in class: derivations, order-of-magnitude estimates with explicit substitutions, and the conceptual clarifications that slides cannot carry. Each slide corresponds to a subsection here. Slides use letters (A, B, C, D) following the outline in the deck; the notes use decimal section numbering (Section 1.1, 1.2, ...).

Three kinds of boxes appear in the text:

- *Derivation* boxes contain the algebraic steps behind a result that is only stated on the slide.
- *Numerical check* boxes substitute typical detector numbers to verify an order of magnitude.
- *Pitfall* boxes flag a point that regularly confuses students at this level.

Each block closes with a short problem set. Solutions are provided in a separate document.

Corrections and suggestions are welcome at `gianluca.gemme@ge.infn.it`.

Chapter 1

Block 1 — Interaction of GWs with Test Masses

Block overview

Block 1 is theoretical. It asks a simple question: given a free system of test masses and a gravitational wave passing through it, what happens, and what is there to measure?

The answer depends on the coordinates we use. The content of the block is organised in four sections:

- **Section 1.1.** Setting the stage. Why the gauge question matters, and a compact recap of the tools needed (TT gauge, linearised Riemann, geodesic deviation).
- **Section 1.2.** The TT-frame picture. Test masses at rest in coordinates, proper distance changing under the wave, and light propagation along an arm, with the emergence of the sinc factor.
- **Section 1.3.** The proper detector frame picture. Fermi normal coordinates, Earth-bound laboratory corrections, and the Newtonian tidal force picture.
- **Section 1.4.** From test masses to detector output. The L-shaped geometry, strain as a differential observable, and antenna patterns.

By the end of Block 1 a student should be able to:

- explain why the same physics looks different in the TT frame and in the proper detector frame, and when each is appropriate;
- compute the proper-distance change between free test masses induced by a GW;
- describe the interferometer response in TT gauge;
- use the Newtonian tidal-force picture in the proper detector frame;
- write down the detector output $h(t) = F_+ h_+ + F_\times h_\times$ and state its geometric meaning.

1.1 Setting the stage — why the gauge question matters

This section exists to avoid a specific form of confusion. When students first meet a GW in the TT gauge, they are told that free test masses "do not move" even though the wave is doing something observable. When they meet the same GW in the proper detector frame, they are told that free test masses *do* move, driven by a Newtonian-looking tidal force. Both statements are standard, both are correct, and on a first pass they look contradictory.

The resolution is the one common to all of General Relativity: coordinates are not observables. The observable is the proper distance (or, in a detector, the round-trip light time), and the two pictures agree on it.

Rather than argue for this in the abstract, the rest of this section sets up the two frames explicitly. Sections 1.2 and 1.3 of this block then use the same mathematical apparatus in each, and confirm that they give the same answer for the quantity a detector can measure.

1.1.1 Gauge freedom: physics invariant, description is not

The Einstein equations are covariant under diffeomorphisms. A change of coordinates does not change the spacetime geometry; it changes the metric components we write down. In the linearised theory an infinitesimal gauge transformation is a change of coordinates $x^\alpha \to x^\alpha + \xi^\alpha$ with $|\partial\xi| \ll 1$, under which the metric perturbation transforms as

$$h_{\alpha\beta} \;\longrightarrow\; h_{\alpha\beta} - \partial_\alpha \xi_\beta - \partial_\beta \xi_\alpha. \tag{1.1}$$

The gauge group has four parameters (ξ^α for $\alpha = 0, 1, 2, 3$) and is used up in two stages: first to impose the Lorenz gauge, and then to fix a residual freedom. At the end of both stages only two components of $h_{\alpha\beta}$ are left. They are the two physical polarizations h_+ and $h_\times$.

Two gauge choices will appear repeatedly:

TT frame.
The gauge that makes the wave simplest. Only the two polarizations appear; the wave is entirely spatial, transverse, and traceless.

Proper detector frame.
The gauge that makes the apparatus simplest. The metric is Minkowski at the origin and deviates from Minkowski further out. Test masses feel deviations from Minkowski as Newtonian-looking forces.

Both gauges give the same answer for any physical observable. They are bookkeeping choices, not physical alternatives.

> **Pitfall.** It is tempting to ask which frame is "real". Neither is. What is real is the output of a physical measurement, for example the round-trip time of a photon along an interferometer arm. Each frame produces the same number for that measurement. The freedom to choose one or the other is the gauge freedom of the theory.

The rest of Section 1.1 collects the tools we will use throughout the block: the TT conditions, the linearised Riemann tensor, and the geodesic-deviation equation. These are recapped, not derived from scratch; any standard GR textbook covers them. Students comfortable with this material can skim the following three subsections and go to Section 1.1.5.

1.1.2 Recap — the TT gauge

Write the metric as $g_{\alpha\beta} = \eta_{\alpha\beta} + h_{\alpha\beta}$ with $|h_{\alpha\beta}| \ll 1$, and define the trace-reversed perturbation

$$\bar{h}_{\alpha\beta} \;\equiv\; h_{\alpha\beta} - \tfrac{1}{2}\,\eta_{\alpha\beta}\,h, \qquad h \equiv \eta^{\alpha\beta} h_{\alpha\beta}. \tag{1.2}$$

Imposing the Lorenz gauge $\partial^\beta \bar{h}_{\alpha\beta} = 0$, the vacuum linearised Einstein equations reduce to

$$\Box\, \bar{h}_{\alpha\beta} = 0. \tag{1.3}$$

Lorenz fixes four components out of the ten in the symmetric matrix $h_{\alpha\beta}$, leaving six. The residual gauge freedom consists of transformations with $\Box\xi^\alpha = 0$; using the four parameters ξ^α we can impose four additional conditions. The standard choice is

$$h_{0\alpha} = 0, \qquad h^i{}_i = 0, \qquad \partial^j h_{ij} = 0. \tag{1.4}$$

The first equation removes all time-like components; the second makes the perturbation traceless; the third makes it transverse to its propagation direction. Because the perturbation is traceless, $\bar{h}_{ij} = h_{ij}$ identically, and we write h^{TT}_{ij} to make the choice of gauge explicit.

Two independent components survive. For a plane wave travelling along $\hat{z}$,

$$h^{\mathrm{TT}}_{ij}(t, z) \;=\; \begin{pmatrix} h_+ & h_\times & 0 \\ h_\times & -h_+ & 0 \\ 0 & 0 & 0 \end{pmatrix} \cos\!\big[\omega_{\mathrm{gw}}(t - z/c)\big]. \tag{1.5}$$

h_+ and $h_\times$ are the two physical polarizations.

Note. The counting of degrees of freedom is worth spelling out once. $h_{\alpha\beta}$ has 10 independent components. Lorenz gauge imposes 4 conditions, leaving 6. The residual gauge transformation has 4 independent parameters ξ^α; the TT conditions (1.4) use all 4 of them. Net: $10-4-4=2$ physical degrees of freedom, matching the two polarizations of a massless spin-2 field.

1.1.3 Recap — the Riemann tensor of a linear GW

At linear order in h the Riemann tensor reads

$$R_{\alpha\beta\gamma\delta} = \tfrac{1}{2}\big(\partial_\beta\partial_\gamma h_{\alpha\delta} + \partial_\alpha\partial_\delta h_{\beta\gamma} - \partial_\alpha\partial_\gamma h_{\beta\delta} - \partial_\beta\partial_\delta h_{\alpha\gamma}\big). \tag{1.6}$$

A direct substitution of the transformation (1.1) into (1.6) gives zero change to all components: at first order in h, the Riemann tensor is gauge invariant. This is the single fact that makes the whole block work. It means that we can compute R in whichever gauge is most convenient (TT, always) and use the result in any other gauge (the proper detector frame, when we get there).

The component that is relevant for geodesic deviation is R_{i0j0}. In TT gauge $h_{00} = h_{0i} = 0$, so of the four terms in (1.6) only the one with two time derivatives on h_{ij} survives:

$$R_{i0j0} \;=\; -\tfrac{1}{2}\,\partial_0^2\, h_{ij}^{\mathrm{TT}} \;=\; -\frac{1}{2c^2}\,\ddot{h}_{ij}^{\mathrm{TT}}, \tag{1.7}$$

where the overdot denotes a derivative with respect to coordinate time t and the factor of c^2 converts from $x^0 = ct$. Raising the first index with η^{ik} does not change the numerical value: the spatial part of η is the Euclidean metric,

$$R^i{}_{0j0} \;=\; \eta^{ik} R_{k0j0} \;=\; R_{i0j0} \;=\; -\frac{1}{2c^2}\,\ddot{h}_{ij}^{\mathrm{TT}}. \tag{1.8}$$

This is the expression that goes into the geodesic-deviation equation next.

1.1.4 Recap — geodesic and geodesic-deviation equations

A free test mass of four-velocity $u^\mu = dx^\mu/d\tau$ follows the geodesic equation,

$$\frac{d^2x^\mu}{d\tau^2} + \Gamma^\mu_{\alpha\beta}\,\frac{dx^\alpha}{d\tau}\,\frac{dx^\beta}{d\tau} \;=\; 0. \tag{1.9}$$

Two free test masses with proper-separation vector ξ^μ satisfy the geodesic-deviation equation,

$$\frac{D^2\xi^\mu}{D\tau^2} \;=\; -\,R^\mu{}_{\alpha\beta\gamma}\,u^\alpha\,\xi^\beta\,u^\gamma. \tag{1.10}$$

We specialise to two test masses initially at rest, so that $u^\mu \simeq (c,\vec{0})$, and work to lowest order in h.

Derivation.

For spatial components with $\xi^0 = 0$ and $u^\mu = (c,\vec{0})$, equation (1.10) reduces to

$$\frac{D^2\xi^i}{D\tau^2} \;=\; -\,R^i{}_{0j0}\,(u^0)^2\,\xi^j \;=\; -\,c^2\,R^i{}_{0j0}\,\xi^j. \tag{1.11}$$

At lowest order in h, the covariant time derivative reduces to the ordinary one: the Christoffel symbols are already $\mathcal{O}(h)$, and they act on a ξ^i whose time evolution is itself $\mathcal{O}(h)$, so the correction is $\mathcal{O}(h^2)$ and can be dropped. Substituting (1.8),

$$\ddot{\xi}^i \;=\; -\,c^2\left(-\tfrac{1}{2c^2}\,\ddot{h}_{ij}^{\mathrm{TT}}\right)\xi^j \;=\; \tfrac{1}{2}\,\ddot{h}_{ij}^{\mathrm{TT}}\,\xi^j. \tag{1.12}$$

The c^2 from the four-velocity and the c^2 from the Riemann tensor cancel out; the remaining equation is manifestly non-relativistic in form.

The result is

$$\boxed{\ddot{\xi}^i \;=\; \tfrac{1}{2}\,\ddot{h}^{\mathrm{TT}}_{ij}\,\xi^j.} \tag{1.13}$$

Integrating twice in time, with the wave turned on adiabatically so that both ξ^i and $\dot{\xi}^i$ vanish initially,

$$\Delta\xi^i(t) \;=\; \tfrac{1}{2}\,h^{\mathrm{TT}}_{ij}(t)\,\xi^j_0, \tag{1.14}$$

where ξ^j_0 is the initial separation. The fractional change in proper separation is of order h.

Pitfall. Equation (1.13) does *not* say that free test masses accelerate in TT coordinates. The ξ^i in the geodesic-deviation equation is a *proper* separation between two worldlines, not a coordinate position. In TT gauge, the coordinate positions of free test masses initially at rest do not change: we will prove this explicitly at the start of Section 1.2. Only their proper separation changes. The distinction matters every time one reasons about what the detector measures.

Equation (1.13) is the master equation of Block 1. In the TT frame it will be used to compute the change in proper separation produced by the wave, and from there the round-trip time of a photon travelling between two test masses. In the proper detector frame the same equation will be re-interpreted as Newton's second law with a tidal gravitational force $F^i = (m/2)\,\ddot{h}^{\mathrm{TT}}_{ij}\,\xi^j$ on the test masses.

A sense of scale: $h{\sim}10^{-21}$ is a typical amplitude for an astrophysical signal. For an arm of $L{\sim}3$ km the proper-separation change is $\Delta L{\sim}(1/2)\,h\,L{\sim}1.5\times10^{-18}$ m. This is the number we will be chasing through the whole of Block 2.

1.1.5 Roadmap: two complementary pictures

The rest of Block 1 applies equation (1.13) in two ways.

In the **TT frame** (Section 1.2), the coordinates are constructed so that free test masses stay at rest in them. Proper separations then change with the wave, and the resulting effect on a photon travelling along an arm is a change in its round-trip time. This is the natural language for light propagation and for situations where the arm length is comparable to the GW wavelength.

In the **proper detector frame** (Section 1.3), the coordinates are built around the worldline of the central test mass using a rigid-ruler construction (Fermi normal coordinates). Free test masses now appear to move, driven by a tidal force. This is the natural language for noise modelling, feedback control, and the mechanics-style reasoning that experimentalists use when designing the instrument.

Both pictures describe the same physics, and their predictions for any physical observable coincide. The long-wavelength limit $\lambda_{\mathrm{gw}} \gg L$ is where the two match most transparently; ground-based detectors sit firmly inside this regime. We return to this explicitly at the end of Section 1.3.

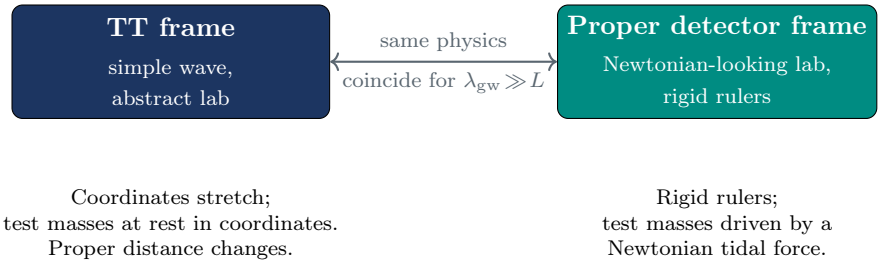

With this machinery in place, Section 1.2 picks up the first of the two pictures.

1.2 The TT-frame picture

Section 1.2 applies the machinery of Section 1.1 to a free system of test masses. The headline result, derived in Subsections 1.2.1 and 1.2.2, is that free test masses stay at rest in TT coordinates while the proper distance between them changes. The rest of the section develops two concrete applications: the deformation of a ring of test masses (1.2.4–1.2.5) and the response of light travelling between two test masses along an interferometer arm (1.2.6–1.2.9). The second of these produces the sinc factor, the central frequency-domain result of Block 1.

1.2.1 Test mass at rest in the TT frame

Consider a free test mass initially at rest in TT coordinates, so that $u^\mu|_{\tau=0} = (c, \vec{0})$. The geodesic equation (1.9) evaluated at $\tau = 0$ reads

$$\left.\frac{d^2x^i}{d\tau^2}\right|_{\tau=0} = -\left.\Gamma^i_{00}\,(u^0)^2\right|_{\tau=0}. \tag{1.15}$$

The relevant Christoffel symbol in linearised form is

$$\Gamma^i_{00} = \tfrac{1}{2}\,\eta^{ij}\big(2\,\partial_0 h_{0j} - \partial_j h_{00}\big). \tag{1.16}$$

In TT gauge $h_{00} = 0$ and $h_{0j} = 0$ not just at the origin but throughout spacetime, so

$$\Gamma^i_{00} \;=\; 0 \qquad \text{identically in TT gauge.} \tag{1.17}$$

At $\tau = 0$ the coordinate velocity $u^i = 0$ and the coordinate acceleration $d^2x^i/d\tau^2 = 0$. Both remain zero at later τ because the only term that could drive them, $\Gamma^i{}_{00}$, vanishes everywhere: a static worldline is an exact solution of the geodesic equation in TT coordinates.

Result. A free test mass initially at rest in TT coordinates remains at rest in TT coordinates for all times, even after the passage of a gravitational wave.

This is the defining property of TT coordinates. The coordinate grid is built, by construction, so that the free test masses mark it: the coordinate labels are glued to the masses.

1.2.2 Physical meaning: coordinates stretch with the wave

"Test masses at rest in coordinates" is a statement about coordinates. It is not a statement that nothing happens. The physics is in the metric.

The spatial metric in TT gauge is $g_{ij} = \delta_{ij} + h^{\mathrm{TT}}_{ij}$. The coordinate positions of two free test masses are fixed, but the proper distance between them is computed from the metric, which oscillates with the wave. Proper distance is the observable quantity; coordinate distance is not.

The same fact can be stated from the other direction. The TT coordinates stretch and squeeze with the wave, exactly in step with the free test masses, so that each mass stays pinned to its coordinate label while the physical separation between labels changes. Whether one thinks of the coordinates as deforming and the masses as fixed, or the other way around, is a matter of taste; both are shorthand for the same geometry.

Pitfall. "Coordinates stay put" does not mean "nothing happens". The next subsection computes the proper distance explicitly and shows that it changes by an amount proportional to h. Whenever a student says "but the test masses do not move", the reply is: move *relative to what*? Relative to TT coordinates, no. Relative to each other (proper distance), yes.

1.2.3 Proper distance between free test masses

Take two free test masses at rest in TT coordinates, with TT-coordinate separation $\xi^i = L\,\hat{n}^i$, where $\hat{n}^i$ is the unit vector along the separation. At time t the proper distance between them along the straight coordinate path is

$$s(t) \;=\; \int_0^L \sqrt{g_{ij}(t)\,dx^i\,dx^j} \;=\; \int_0^L d\sigma\,\sqrt{1 + h^{\rm TT}_{ij}(t)\,\hat{n}^i\hat{n}^j}, \tag{1.18}$$

where σ parametrises the path and $dx^i = \hat{n}^i\,d\sigma$. In the long-wavelength limit $h^{\rm TT}_{ij}$ is approximately constant along the path at fixed t; expanding to first order in h,

$$s(t) \;\simeq\; L\left[1 + \tfrac{1}{2}\,h^{\rm TT}_{ij}(t)\,\hat{n}^i\hat{n}^j\right]. \tag{1.19}$$

The fractional change is

$$\boxed{\frac{\Delta s(t)}{L} \;=\; \tfrac{1}{2}\,h^{\rm TT}_{ij}(t)\,\hat{n}^i\hat{n}^j.} \tag{1.20}$$

Note. The quasi-static approximation (h_{ij} constant along the path) is good as long as the photon/ruler traverses the path in a time short compared with the GW period, i.e. $L/c \ll 1/f_{\rm gw}$. For $L = 3$ km and $f_{\rm gw} \lesssim 10$ kHz, $L/c{\sim}10^{-5}$ s and $1/f_{\rm gw} \gtrsim 10^{-4}$ s, so this is safe. The full calculation in Subsection 1.2.7 quantifies the correction.

Equation (1.20) matches the result of the geodesic-deviation equation (1.13): integrating $\ddot{\xi}^i = (1/2)\,\ddot{h}^{\rm TT}_{ij}\,\xi^j$ twice in time and identifying the proper separation with ξ^i (valid at leading order in h) gives $\Delta\xi^i = (1/2)\,h^{\rm TT}_{ij}\,\xi^j$. Projecting along $\hat{n}$ reproduces (1.20).

1.2.4 Effect on a ring of test masses: plus polarization

Take a wave propagating along $\hat{z}$ with pure h_+ polarization ($h_\times = 0$):

$$h^{\rm TT}_{ij}(t) \;=\; h_+(t)\begin{pmatrix}1 & 0 & 0\\ 0 & -1 & 0\\ 0 & 0 & 0\end{pmatrix}, \qquad h_+(t) = h_0\cos(\omega_{\rm gw}t). \tag{1.21}$$

A test mass with initial TT-coordinate separation $\xi^i = (x_0, y_0, 0)$ from the origin has a proper-separation change (1.14)

$$\Delta x \;=\; \tfrac{1}{2}\,h_+(t)\,x_0, \qquad \Delta y \;=\; -\tfrac{1}{2}\,h_+(t)\,y_0. \tag{1.22}$$

A ring of test masses of radius R in the xy-plane is therefore deformed into an ellipse with semi-axes $R\,[1 + h_+(t)/2]$ along $\hat{x}$ and $R\,[1 - h_+(t)/2]$ along $\hat{y}$. Over a full period of the wave the ring returns to its original shape twice: stretched along $\hat{x}$ and squeezed along $\hat{y}$ at $t = 0$, circular at $t = T/4$, stretched along $\hat{y}$ and squeezed along $\hat{x}$ at $t = T/2$, circular again at $t = 3T/4$.

The pattern is quadrupolar, which is why the gravitational wave is a spin-2 field and the detector geometry is L-shaped rather than pencil-shaped.

1.2.5 Effect on a ring of test masses: cross polarization

For pure $h_\times$ polarization,

$$h^{\rm TT}_{ij}(t) \;=\; h_\times(t)\begin{pmatrix}0 & 1 & 0\\ 1 & 0 & 0\\ 0 & 0 & 0\end{pmatrix}, \tag{1.23}$$

and

$$\Delta x \;=\; \tfrac{1}{2}\, h_\times(t)\, y_0, \qquad \Delta y \;=\; \tfrac{1}{2}\, h_\times(t)\, x_0. \tag{1.24}$$

A ring of test masses is deformed into an ellipse with principal axes along the diagonals $\hat{x} \pm \hat{y}$, rotated by 45° with respect to the h_+ case.

The two polarizations h_+ and $h_\times$ are linearly independent, and a general plane wave is a superposition of both. A single L-shaped detector with arms along $\hat{x}$ and $\hat{y}$ responds differently to the two: it is maximally sensitive to h_+ and completely blind to $h_\times$ for a wave from zenith. Subsection 1.4.3 formalises this into the antenna-pattern functions F_+ and $F_\times$.

1.2.6 Light propagation along one arm: setup

The detector does not observe proper distance directly. It measures the *round-trip time* of light travelling along its arms. The next three subsections compute this round-trip time in TT gauge, to first order in h.

Take one arm along $\hat{x}$, with the input mirror at the TT-coordinate origin and the end mirror at TT-coordinate position $L\hat{x}$. A wave h_+ propagates along $\hat{z}$, so that along the arm $h^{\mathrm{TT}}_{xx}(t) = h(t)$, where we drop the subscript from here on. Only the xx component of the metric is relevant; the spatial metric along the arm reads

$$ds^2 \;=\; -\,c^2\, dt^2 + \big[1 + h(t)\big]\, dx^2, \tag{1.25}$$

where the time dependence of h is evaluated at the photon location at time t (not at $t = 0$).

For a null geodesic, $ds^2 = 0$, hence

$$c\, dt \;=\; \sqrt{1 + h(t)}\; dx \;\simeq\; \Big[1 + \tfrac{1}{2}\, h(t)\Big]\, dx, \tag{1.26}$$

to first order in h. The photon travel time is the integral of this relation along the arm.

> **Note.** The integration limits for a photon that goes from the input mirror to the end mirror are 0 and L, *exactly*. The mirrors are free test masses and their coordinate positions do not change in TT gauge (Subsection 1.2.1). All of the effect of the wave enters through the metric coefficient $\sqrt{1 + h(t)}$ in front of dx, not through the endpoints.

1.2.7 Round-trip time: the sinc factor

For a monochromatic wave $h(t) = h_0 \cos(\omega_{\mathrm{gw}} t)$, the travel time from the input mirror at t_0 to the end mirror is

$$t_1(t_0) - \frac{L}{c} \;=\; \frac{1}{2c} \int_0^L h\big(t_0 + x/c\big)\, dx. \tag{1.27}$$

Derivation.

Carry out the integral:

$$\frac{1}{2c} \int_0^L h_0 \cos\big[\omega_{\mathrm{gw}}(t_0 + x/c)\big]\, dx = \frac{h_0}{2\omega_{\mathrm{gw}}} \Big[\sin\big(\omega_{\mathrm{gw}}(t_0 + L/c)\big) - \sin(\omega_{\mathrm{gw}} t_0)\Big] \tag{1.28}$$

$$= \frac{h_0}{\omega_{\mathrm{gw}}}\, \sin\Big(\tfrac{\omega_{\mathrm{gw}} L}{2c}\Big)\, \cos\Big[\omega_{\mathrm{gw}}\Big(t_0 + \tfrac{L}{2c}\Big)\Big], \tag{1.29}$$

using the sum-to-product identity $\sin A - \sin B = 2\cos\frac{A+B}{2}\sin\frac{A-B}{2}$. Writing the result in

terms of $\mathrm{sinc}(x) \equiv \sin x/x$,

$$t_1(t_0) - \frac{L}{c} \;=\; \frac{L\,h_0}{2c}\,\mathrm{sinc}\!\left(\tfrac{\omega_{\rm gw}L}{2c}\right)\,\cos\!\left[\omega_{\rm gw}\!\left(t_0 + \tfrac{L}{2c}\right)\right]. \tag{1.30}$$

The return trip from the end mirror at time t_1 back to the input mirror follows the same calculation with $t_0 \to t_1 \simeq t_0 + L/c$:

$$t_2 - \frac{L}{c} \;=\; \frac{L\,h_0}{2c}\,\mathrm{sinc}\!\left(\tfrac{\omega_{\rm gw}L}{2c}\right)\,\cos\!\left[\omega_{\rm gw}\!\left(t_0 + \tfrac{3L}{2c}\right)\right]. \tag{1.31}$$

Summing the two and using $\cos A + \cos B = 2\cos\frac{A+B}{2}\cos\frac{A-B}{2}$,

$$t_{\rm rt}(t_0) - \frac{2L}{c} \;=\; \frac{L\,h_0}{c}\,\mathrm{sinc}\!\left(\tfrac{\omega_{\rm gw}L}{2c}\right)\cos\!\left(\tfrac{\omega_{\rm gw}L}{2c}\right)\,\cos\!\left[\omega_{\rm gw}(t_0 + L/c)\right]. \tag{1.32}$$

The product $\mathrm{sinc}(x)\cos(x) = \sin(2x)/(2x) = \mathrm{sinc}(2x)$ simplifies the frequency-dependent factor:

$$\boxed{t_{\rm rt}(t_0) - \frac{2L}{c} \;=\; \frac{L\,h_0}{c}\,\mathrm{sinc}\!\left(\tfrac{\omega_{\rm gw}L}{c}\right)\,\cos\!\left[\omega_{\rm gw}(t_0 + L/c)\right].} \tag{1.33}$$

Three features of this result are worth noting.

Linear in h_0. The round-trip time shift is proportional to the GW amplitude. The interferometer is a linear transducer from h to travel time, to first order.

Proportional to L. The prefactor L/c says that the absolute travel-time shift scales with the arm length. Longer arms give a larger signal. This is the reason to build kilometre-scale arms, not centimetre-scale ones.

Frequency-dependent sinc factor. The argument of the sinc is $\omega_{\rm gw}L/c$ for the round trip, which is twice the argument $\omega_{\rm gw}L/(2c)$ of the one-way sinc in (1.30). The factor of 2 comes from the round trip and the $\sin(2x) = 2\sin x\cos x$ identity; see Exercise 3.

1.2.8 Regimes of the sinc factor

The function $\mathrm{sinc}(\omega_{\rm gw}L/c)$ controls the frequency response of the arm. Two limits and one discrete set of special points:

Long-wavelength limit ($\lambda_{\rm gw} \gg L$, or equivalently $\omega_{\rm gw}L/c \ll 1$). The sinc tends to 1 and the round-trip response becomes frequency-independent: $\Delta t_{\rm rt} \simeq h\,L/c$. The arm behaves as if it were instantaneously stretched by the wave, and the photon picks up an extra travel time equal to h times the transit time L/c. This is the regime in which all current ground-based detectors operate.

Short-wavelength limit ($\lambda_{\rm gw} \ll L$). The sinc tends to zero. The wave oscillates many times during one photon transit, and the contributions from different parts of the arm average to zero. The arm becomes insensitive to the wave.

Zero crossings. $\mathrm{sinc}(x) = 0$ at $x = n\pi$, so the round-trip response vanishes at $f_{\rm gw} = n\,c/(2L)$ for $n = 1, 2, \ldots$.

Numerical check. For Virgo and LIGO, $L = 3$–4 km gives a first zero at $f = c/(2L) \simeq 38$–50 kHz. For Einstein Telescope's 10 km arms, the first zero is at $\simeq 15$ kHz. The detection band of all these detectors (10 Hz to ∼10 kHz) sits inside the first lobe of the sinc, where the function is close to unity. The sinc factor is therefore a small correction for ground-based detectors.

For LISA, with arm length $L \simeq 2.5 \times 10^6$ km and detection band 0.1 mHz to 1 Hz, $c/(2L) \simeq 60$ mHz sits inside the detection band. The LISA response is deep in the sinc regime, and special analysis is required.

1.2.9 Audio sidebands at the output

The laser field at the input mirror is $A_{\rm in}(t) = A_0\, e^{-i\omega_L t}$. After one round trip the field returning to the input mirror at time t is the input field at the emission time $t - t_{\rm rt}(t)$:

$$A_{\rm out}(t) \;=\; A_0\, e^{-i\omega_L\,[t - t_{\rm rt}(t)]}. \tag{1.34}$$

Expanding $t_{\rm rt}(t) = 2L/c + \Delta t_{\rm rt}(t)$ with $\Delta t_{\rm rt}$ given by (1.33), and keeping first order in h_0,

$$A_{\rm out}(t) \;=\; A_0\, e^{-i\omega_L(t-2L/c)}\left[1 + i\omega_L\,\Delta t_{\rm rt}(t) + O(h_0^2)\right]. \tag{1.35}$$

Writing the cosine in $\Delta t_{\rm rt}$ as a sum of exponentials,

$$A_{\rm out}(t) \;=\; A_0\, e^{-i\omega_L(t-2L/c)}\left[1 + \tfrac{i}{2}\,h_0\,k_L L\,\mathrm{sinc}\!\left(\tfrac{\omega_{\rm gw}L}{c}\right)\left(e^{i\omega_{\rm gw}(t-L/c)} + e^{-i\omega_{\rm gw}(t-L/c)}\right)\right], \tag{1.36}$$

where $k_L = \omega_L/c$ is the laser wavenumber.

Equation (1.36) is the input–output relation of a single arm, to first order in h_0. It contains:

- a **carrier** at the laser frequency ω_L, with phase $2k_L L$ from the static round-trip propagation;
- two **audio sidebands** at $\omega_L \pm \omega_{\rm gw}$, with amplitude proportional to $h_0\, k_L L\,\mathrm{sinc}(\omega_{\rm gw}L/c)$.

The sideband amplitude is linear in L through the factor $k_L L = 2\pi L/\lambda_L$. The number of laser wavelengths fitted inside the arm is a design parameter: more wavelengths means a larger signal.

Reading out the signal at the photodiode is a question of measuring the beat between the carrier and the sidebands. The details (dark-fringe operation, RF or DC readout, balanced homodyne) belong to Block 2 and to dedicated school lectures on optical configurations (A. Perreca, Fri 22 & Sat 23).

> **Note.** In the Michelson topology, the carrier at the dark port is nominally suppressed by destructive interference between the two arms, while the sidebands produced by a differential h are recombined constructively. A real detector reintroduces a small amount of carrier at the dark port (by a DC offset, or by RF sidebands on the input light) to beat against the GW sidebands and produce a photocurrent linear in h_0 at the photodiode. We return to this in Section 2.1.

1.3 The proper detector frame picture

Section 1.2 described the effect of a GW on a system of free test masses in TT coordinates. The physics is fine but the language does not match the way an experimentalist describes a laboratory. In a lab, positions are marked with rigid rulers anchored to a fixed origin, and we expect the test masses to *move* when a GW passes through. Section 1.3 builds a set of coordinates that realise this expectation: the proper detector frame.

The proper detector frame is a local coordinate system, valid only in a tube of size small compared with the curvature scale of the wave. For ground-based detectors this is an excellent approximation (Subsection 1.3.7). Inside the tube the metric is Minkowski at the origin plus corrections organised in an expansion in r/L_B, where L_B is the curvature scale. The corrections have a clean physical interpretation: Newtonian gravity, centrifugal and Coriolis pseudo-forces, and the GW tidal force.

1.3.1 Why experimentalists use a different frame

When a mechanical engineer designs the Virgo superattenuator, or when a control engineer writes the feedback loop for the interferometer longitudinal degrees of freedom, neither of them thinks in TT coordinates. They think in terms of a fixed reference frame attached to the laboratory, rigid rulers aligned with the beams, and forces acting on mirrors.

This is the frame we want to construct. It has three characteristic features:

- Coordinates are built around a central worldline (typically the worldline of the beam splitter), so that the origin is always on that worldline.
- Spatial axes are orthogonal and rigid at the origin. Rulers can be calibrated against them.
- Free test masses at non-zero coordinate position *do* move under the action of a GW, driven by a tidal force that plays the role of gravity in Newton's second law.

The mathematical object that realises these features for a free-falling central worldline is called Fermi normal coordinates; for a non-inertial worldline (accelerated, rotating) one adds further corrections. The next three subsections write the metric explicitly.

1.3.2 Fermi normal coordinates: free-falling lab

The construction of Fermi normal coordinates starts from a reference worldline $\gamma(\tau)$ parametrised by its proper time τ, with an orthonormal tetrad $e^{\mu}_{(a)}$ Fermi-Walker transported along it. The coordinate t is the proper time of the central observer, and the spatial coordinates x^i are proper distances along the spatial tetrad legs at fixed t. The metric is Minkowski at every point of the central worldline, $\Gamma^{\alpha}{}_{\beta\gamma}$ vanishes there, and the corrections off the worldline are organised in a power series in the spatial distance $r = \sqrt{\delta_{ij}x^i x^j}$.

To second order in r,

$$\begin{aligned} ds^2 \;=\; & -c^2\,dt^2\left[1 + R_{0i0j}\,x^i x^j\right] - 2\,c\,dt\,dx^i\left[\tfrac{2}{3}\,R_{0jik}\,x^j x^k\right] \\ & + dx^i\,dx^j\left[\delta_{ij} - \tfrac{1}{3}\,R_{ikjl}\,x^k x^l\right], \end{aligned} \tag{1.37}$$

where the Riemann-tensor components are evaluated on the central worldline. At the origin ($x^i = 0$) the metric is Minkowski and all Christoffel symbols vanish: by the equivalence principle, physics at the origin of a freely-falling lab is special-relativistic.

The Riemann tensor in (1.37) is the full one, including static tidal effects from the Earth, the Moon, and other slow sources, as well as the GW contribution we want. Separating the two is a matter of frequency: the detector band (10 Hz to 10 kHz) is far above the frequencies of all static and quasi-static tidal effects.

Note. The validity of the expansion (1.37) requires $r \ll L_B$, where L_B is the curvature scale. For the GW contribution, $L_B \sim \lambda_{\rm gw}$, so the expansion is valid as long as the detector is much smaller than the GW wavelength. Subsection 1.3.7 makes this quantitative for ground-based detectors.

1.3.3 Earth-bound lab: adding acceleration and rotation

Equation (1.37) describes a free-falling observer. A real laboratory on Earth is not in free fall: it sits on the Earth's surface, supported against local gravity (coordinate acceleration $\mathbf{a} = -\mathbf{g}$) and rotating with the Earth (angular velocity $\mathbf{\Omega}$). Transforming from the local free-falling frame

to the Earth-bound one is a standard but tedious calculation; the result is the *proper detector frame* metric,

$$\begin{aligned} ds^2 \;=\; & -c^2dt^2\left[1+\tfrac{2}{c^2}\,\mathbf{a}\cdot\mathbf{x}+\tfrac{1}{c^4}(\mathbf{a}\cdot\mathbf{x})^2-\tfrac{1}{c^2}(\boldsymbol{\Omega}\times\mathbf{x})^2+R_{0i0j}\,x^ix^j\right] \\ & +2\,c\,dt\,dx^i\left[\tfrac{1}{c}\,\epsilon_{ijk}\,\Omega^j x^k-\tfrac{2}{3}\,R_{0jik}\,x^jx^k\right] \\ & +dx^i\,dx^j\left[\delta_{ij}-\tfrac{1}{3}\,R_{ikjl}\,x^kx^l\right]. \end{aligned} \tag{1.38}$$

This is the metric for Subsection 1.3.4. No new physics is added: only the description of a laboratory that is accelerating and rotating in a locally free-falling environment.

We will not derive (1.38) in detail; the individual corrections are recognisable from Newtonian physics, once interpreted in the right order in r.

1.3.4 Hierarchy of corrections in r/L_B

The proper detector frame metric (1.38) contains corrections of different orders in r:

Order r^0. The zero-distance limit: flat Minkowski metric. A mass at the origin obeys special relativity.

Order r^1. The terms linear in $\mathbf{x}$: $\mathbf{a}\cdot\mathbf{x}$ and $\epsilon_{ijk}\Omega^jx^k$. These produce the Newtonian uniform gravitational field $\mathbf{g}=-\mathbf{a}$, the centrifugal potential $-(1/2)(\boldsymbol{\Omega}\times\mathbf{x})^2$, and the Coriolis pseudo-force. These are the standard non-inertial corrections of a rotating, accelerating lab. They are present whether or not a GW is passing through.

Order r^2. The Riemann-tensor terms: $R_{0i0j}\,x^ix^j$, $R_{0jik}\,x^jx^k$, $R_{ikjl}\,x^kx^l$. These describe tidal effects. The Riemann tensor contains both the static (Earth, Moon, Sun) and the GW contributions.

The r^1 terms are huge compared with the r^2 terms of the GW: $\mathbf{a}\cdot\mathbf{x}\sim gL\sim 3\times10^4\,\mathrm{m^2/s^2}$ for $L=3$ km, while the GW term scales like $c^2R\,L^2\sim\ddot{h}\,L^2\sim\omega^2hL^2\sim10^{-11}\,\mathrm{m^2/s^2}$ for $h\sim10^{-21}$ and $\omega\sim2\pi\cdot100$ rad/s. Fifteen orders of magnitude separate the two.

Why detectors can see GWs at all. The static and r^1 corrections are huge, but they are DC or at most slowly varying (tides, Earth rotation). GWs oscillate at 10 Hz to 10 kHz, far above these time scales. The static and slow parts can be suppressed by a mechanical suspension (Section 2.3), leaving the high-frequency GW contribution essentially untouched. Frequency separation is the reason the whole enterprise works.

1.3.5 The Newtonian-force picture

Inside the detector band, all slowly varying effects have been suppressed: gravity is compensated by the suspensions, Earth rotation is DC, static tides are well below 10 Hz. The only surviving piece of the Riemann tensor is the GW part,

$$R^i{}_{0j0} \;=\; -\frac{1}{2c^2}\,\ddot{h}^{\mathrm{TT}}_{ij}. \tag{1.39}$$

The geodesic-deviation equation then reduces to

$$\ddot{\xi}^i \;=\; -c^2\,R^i{}_{0j0}\,\xi^j \;=\; \tfrac{1}{2}\,\ddot{h}^{\mathrm{TT}}_{ij}\,\xi^j, \tag{1.40}$$

which, multiplied by the mass, reads

$$\boxed{F^i \;=\; m\,\ddot{\xi}^{\,i} \;=\; \tfrac{m}{2}\,\ddot{h}^{\mathrm{TT}}_{ij}\,\xi^j.} \tag{1.41}$$

This is Newton's second law with a tidal force that acts on each test mass, proportional to its distance from the origin and to the second time derivative of the GW strain.

The proper detector frame is the natural setting for everything an experimentalist does with the instrument. The mirrors are test masses (in the sense of (1.41)), suspended from a chain of pendulums acting as seismic filters. The control loops close around mirror positions in this frame. The noise budget (Block 2) is computed in this frame. GR enters only through the prescription of the driving force (1.41); once that force is known, the rest is Newtonian mechanics.

1.3.6 Ring of test masses: revisited in the force picture

Return to the ring of test masses of Subsection 1.2.4, now in the proper detector frame. For a wave h_+ propagating along $\hat{z}$, the tidal force (1.41) on a mass at position $(x_0, y_0, 0)$ is

$$F_x = \tfrac{m}{2}\,\ddot{h}_+(t)\,x_0, \qquad F_y = -\,\tfrac{m}{2}\,\ddot{h}_+(t)\,y_0. \tag{1.42}$$

The force pattern is quadrupolar: masses on the $\hat{x}$ axis are pushed outward, masses on the $\hat{y}$ axis are pulled inward (when $\ddot{h}_+ > 0$), and vice versa a quarter period later.

The observable displacement of a test mass under this force matches the TT-coordinate result, provided one integrates twice in time. For a monochromatic wave $h_+(t) = h_0 \cos(\omega_{\rm gw} t)$, integration of $\ddot{\xi} = (1/2)\,\ddot{h}\,\xi_0$ gives $\xi(t) = \xi_0 + (1/2)\,h(t)\,\xi_0 + \mathcal{O}(h^2)$, reproducing the ring deformation of Subsection 1.2.4. The two pictures agree on the observable quantity (the position of each test mass relative to the origin) while differing on what they call the mass "doing": in TT, the mass is at rest in coordinates; in the proper detector frame, the mass is oscillating under a Newtonian-looking force. The proper separation between any two masses is the same in both descriptions.

1.3.7 Validity and limits of the two pictures

The two pictures are not equivalent for all detector configurations. The proper detector frame is a local construction valid only inside a tube of size $r \ll L_B$, with $L_B \sim \lambda_{\rm gw}$ for the GW part of the Riemann tensor. When $r \gtrsim L_B$, the quadratic expansion in r/L_B that underlies (1.38) breaks down, and one must go back to TT (or another suitable gauge) to do physics.

Numerical check. *Ground-based detectors.* $L \simeq$ 3–10 km, detection band 10 Hz to 10 kHz. GW wavelengths $\lambda_{\rm gw} = c/f_{\rm gw} \simeq$ 30 km to 30,000 km. Ratio $L/\lambda_{\rm gw} \lesssim 1/3$ at the worst case (ET at 10 kHz). The proper detector frame is safe, and the TT calculation of Subsection 1.2.7 gives sinc $\simeq 1$, matching the Newtonian-force picture.

LISA. $L \simeq 2.5 \times 10^6$ km, detection band 0.1 mHz to 1 Hz. GW wavelengths $\lambda_{\rm gw} \simeq 3 \times 10^5$ to 3×10^9 km. Ratio $L/\lambda_{\rm gw}$ ranges from $\sim 10^{-3}$ to nearly unity and even above. The Newtonian-force picture is not applicable across the whole LISA band; the full TT calculation is necessary, and time-delay interferometry is built on it.

Pulsar timing. Baselines are kpc to Gpc. GW wavelengths (nHz band) are pc to Mpc. Baselines and wavelengths are comparable: the proper detector frame is not applicable at all. The full TT calculation, including retarded-time effects between pulsars, is mandatory.

Rule of thumb. Use the proper detector frame for noise modelling, suspensions, control loops, and anything that reduces to Newtonian mechanics. Use TT gauge for light propagation and for detectors comparable in size with the GW wavelength.

1.4 From test masses to detector output

Sections 1.2 and 1.3 computed the response of a single pair of test masses to a GW. The detector is an L-shaped combination of two such pairs: corner mass at the origin, end masses at distance L along two orthogonal directions. Section 1.4 assembles the L-shape response, defines the strain

$h(t)$ as the differential observable, and shows how the geometry of the source with respect to the detector projects the two polarizations onto a single scalar output through the antenna-pattern functions F_+ and $F_\times$. The section closes with the bridge to Block 2: the interferometer design problem.

1.4.1 L-shaped detector: differential response

Take two orthogonal arms along $\hat{n}_x = \hat{x}$ and $\hat{n}_y = \hat{y}$, sharing a corner mass at the origin, end masses at TT-coordinate positions $L\hat{x}$ and $L\hat{y}$. From (1.20), the proper-length change of each arm is

$$\frac{\Delta L_x(t)}{L} \;=\; \tfrac{1}{2}\, h_{ij}^{\mathrm{TT}}(t)\, \hat{x}^i\, \hat{x}^j \;=\; \tfrac{1}{2}\, h_{xx}^{\mathrm{TT}}(t), \qquad \frac{\Delta L_y(t)}{L} \;=\; \tfrac{1}{2}\, h_{yy}^{\mathrm{TT}}(t). \tag{1.43}$$

For a plane wave propagating along $\hat{z}$, traceless-ness implies $h_{yy}^{\mathrm{TT}} = -h_{xx}^{\mathrm{TT}}$, so the two arm-length changes are equal and opposite, and the differential combination is

$$\Delta L_x(t) - \Delta L_y(t) \;=\; L\, h_{xx}^{\mathrm{TT}}(t). \tag{1.44}$$

The differential combination doubles the signal, relative to a single arm, and cancels any disturbance that acts identically on the two arms (laser frequency fluctuations, uniform temperature drifts, common-mode seismic motion of the corner station). This is the single reason the Michelson topology is the basis of every ground-based GW detector.

1.4.2 Strain: the dimensionless observable

Define the **strain** as the differential arm-length change normalised to the arm length:

$$\boxed{h(t) \;\equiv\; \frac{\Delta L_x(t) - \Delta L_y(t)}{L}.} \tag{1.45}$$

The definition makes $h(t)$ dimensionless. For a wave with pure h_+ polarization and propagation along $\hat{z}$, $h(t) = h_+(t)$.

Numerical check. For a binary neutron-star coalescence at $\sim$100 Mpc distance, the peak strain is $h{\sim}10^{-21}$. For $L = 3$ km arms, the differential arm-length change is

$$\Delta L \;\sim\; h\, L \;\sim\; 10^{-21} \cdot 3 \times 10^{3}\,\mathrm{m} \;\sim\; 3 \times 10^{-18}\,\mathrm{m}. \tag{1.46}$$

Compare this with:

- classical electron radius: 2.8×10^{-15} m;
- proton charge radius: 0.8×10^{-15} m;
- wavelength of the 1064 nm detection laser: 1.064×10^{-6} m.

The target differential length change is three orders of magnitude smaller than a proton, and twelve orders of magnitude smaller than the laser wavelength. All of the engineering of the interferometer exists to turn these numbers into an observable optical signal.

Take-away number. $h{\sim}10^{-21}$ at $L{\sim}3$ km gives $\Delta L{\sim}3 \times 10^{-18}$ m. This is the measurement target for Block 2.

1.4.3 Detector tensor and antenna pattern functions

The differential output of an L-shaped detector can be written as a contraction of the GW perturbation with a geometric object that knows about the arm directions. Define the **detector tensor**

$$D^{ij} \equiv \tfrac{1}{2}\left(\hat{n}_x^i \hat{n}_x^j - \hat{n}_y^i \hat{n}_y^j\right), \tag{1.47}$$

where $\hat{n}_x$ and $\hat{n}_y$ are the unit vectors along the two arms. The strain is then

$$h(t) = D^{ij} h_{ij}^{\mathrm{TT}}(t). \tag{1.48}$$

Now introduce the source frame. The wave propagates along a direction $\hat{k}$ described by two angles (θ, ϕ) in the detector-fixed frame. In the plane orthogonal to $\hat{k}$, pick two polarization basis tensors $e_{ij}^{+}(\hat{k}, \psi)$ and $e_{ij}^{\times}(\hat{k}, \psi)$ constructed from unit vectors in that plane, with ψ the polarization angle that rotates the basis. Any plane-wave h_{ij}^{TT} can be decomposed as

$$h_{ij}^{\mathrm{TT}}(t) = h_{+}(t)\, e_{ij}^{+} + h_{\times}(t)\, e_{ij}^{\times}. \tag{1.49}$$

The detector output therefore reads

$$\boxed{h(t) = F_{+}(\theta, \phi, \psi)\, h_{+}(t) + F_{\times}(\theta, \phi, \psi)\, h_{\times}(t),} \tag{1.50}$$

with the **antenna pattern functions**

$$F_{+} \equiv D^{ij} e_{ij}^{+}, \qquad F_{\times} \equiv D^{ij} e_{ij}^{\times}. \tag{1.51}$$

Explicit calculation of the pattern functions in the standard convention yields

$$F_{+}(\theta, \phi, \psi) = \tfrac{1}{2}(1 + \cos^2\theta)\cos 2\phi \cos 2\psi - \cos\theta \sin 2\phi \sin 2\psi, \tag{1.52}$$

$$F_{\times}(\theta, \phi, \psi) = \tfrac{1}{2}(1 + \cos^2\theta)\cos 2\phi \sin 2\psi + \cos\theta \sin 2\phi \cos 2\psi. \tag{1.53}$$

These are quadrupolar in the angle ϕ around the detector normal, with four maxima and four minima per rotation. The sum $F_{+}^2 + F_{\times}^2$ is independent of the polarization angle ψ and gives the overall directional sensitivity of the detector.

Note. The factor of 1/2 in the definition (1.47) is conventional and matches the 1/2 in (1.20). Some references absorb it into h_{ij}^{TT} or into the polarization basis tensors; cross-checking conventions is essential when comparing literature values of F_{+} and $F_{\times}$.

1.4.4 The fundamental detector output

Equation (1.50) is the single most useful result of Block 1. It says that a single L-shaped detector measures one linear combination of the two GW polarizations, weighted by the geometry of the source in the detector frame. Three consequences:

Polarization is not disentangled. A single detector cannot separate h_{+} from $h_{\times}$. Any measured $h(t)$ is consistent with infinitely many $(h_{+}, h_{\times}, \theta, \phi, \psi)$ tuples.

Sky localisation requires a network. Two detectors with different orientations give two linear combinations of h_{+} and $h_{\times}$, weighted by distinct $F_{+}^{(a)}, F_{\times}^{(a)}$. Three or more detectors with non-degenerate orientations can reconstruct $(h_{+}, h_{\times})$ up to residual degeneracies, along with the source direction through the arrival-time differences between detectors.

Detector orientation is a design choice. Where you put the detector on Earth, and along which compass directions its arms point, determines its antenna pattern. Maximising the uniformity of sky coverage for a network is a geometry problem. This drives the coordinates of KAGRA in Kamioka, LIGO-India in Aundha, and the proposed sites for Einstein Telescope.

1.4.5 Geometry: orientation, sky location, polarization

The angles in (1.50) have clear geometric meanings.

- θ: the angle between the source direction and the normal to the detector plane. $\theta = 0$ means the source is directly overhead.
- ϕ: the azimuth of the source direction in the plane of the detector, measured from the bisector of the arms.
- ψ: the polarization angle, which rotates the $(e^+, e^\times)$ basis in the plane orthogonal to the propagation direction.

The best directional response is for a source at zenith ($\theta = 0$), perpendicular to the detector plane. Inspecting (1.52) and (1.53) at $\theta = 0$: $F_+ = \cos 2\phi \cos 2\psi$ and $F_\times = \cos 2\phi \sin 2\psi$, so $F_+^2 + F_\times^2 = \cos^2 2\phi$. The response still has a quadrupolar dependence on the azimuth, but averaged over ϕ it is $1/2$.

The blind spots are along the bisectors of the arms in the detector plane ($\theta = \pi/2$, $\phi = \pi/4 + n\pi/2$), where both F_+ and $F_\times$ vanish. Between maxima and blind spots, the antenna pattern has the familiar "peanut" shape when plotted on the sphere, with four lobes along the arms.

Over the course of a sidereal day, the rotation of the Earth sweeps (θ, ϕ) for a fixed source through a range of values. For short-duration signals (the ∼second durations of compact binary mergers) this rotation is negligible and the pattern functions are effectively constant. For long-duration signals (continuous waves from spinning neutron stars, hours-long EMRIs in LISA), the rotation modulates the amplitude and frequency of the signal, and is a diagnostic for sky location.

1.4.6 Bridge to Block 2

At the end of Block 1 we have:

- A clear definition of the detector output: $h(t) = F_+(\theta, \phi, \psi)\, h_+(t) + F_\times(\theta, \phi, \psi)\, h_\times(t)$.
- A linear optical response of a single arm to $h(t)$: audio sidebands at $\omega_L \pm \omega_{\rm gw}$ with amplitude proportional to $h_0\, k_L L\, \mathrm{sinc}(\omega_{\rm gw} L/c)$ around a laser carrier.
- A clean mechanical interpretation in the proper detector frame: mirrors are free test masses driven by a Newtonian-looking tidal force $F^i = (m/2)\, \ddot{h}^{\rm TT}_{ij}\, \xi^j$.

Block 2 is about the instrument that reads this signal out of the noise floor. The open questions are concrete:

- How is the single-arm response combined between the two arms to isolate the differential signal? (Michelson topology, dark-fringe operation.)
- How is the signal amplitude boosted to usable levels given the target $h{\sim}10^{-23}/\sqrt{\rm Hz}$? (Fabry–Perot arm cavities, power recycling, signal recycling, squeezing.)
- What are the fundamental noise sources that limit $h(f)$ at each frequency? (Seismic, Newtonian, thermal, quantum.)
- How does a single-detector $h(t)$ become an astrophysical measurement? (Network, sky localisation, multi-messenger follow-up.)

These are the four sections of Block 2.

Block 1 — Summary

- **Gauge matters for the description, not for the physics.** TT frame and proper detector frame give the same observables in the long-wavelength limit $\lambda_{\rm gw} \gg L$, which covers all current ground-based detectors.
- **TT frame.** Free test masses stay at rest in coordinates, by construction. The proper distance between them changes according to $\Delta s/L = (1/2)\, h_{ij}^{\rm TT}\, \hat{n}^i \hat{n}^j$.
- **Light propagation in TT.** The round-trip time of a photon along an arm of length L acquires a correction $\Delta t_{\rm rt} = (L/c)\, h\, \mathrm{sinc}(\omega_{\rm gw} L/c)$, producing audio sidebands at $\omega_L \pm \omega_{\rm gw}$ around the laser carrier.
- **Proper detector frame.** Free test masses are driven by a Newtonian-looking tidal force $F^i = (m/2)\, \ddot{h}_{ij}^{\rm TT}\, \xi^j$. This is the frame for noise modelling and control.
- **Detector output.** $h(t) = F_+(\theta,\phi,\psi)\, h_+(t) + F_\times(\theta,\phi,\psi)\, h_\times(t)$. One detector measures a single linear combination of the two polarizations, weighted by geometry. A network is necessary to disentangle the two polarizations and localise the source.

Block 1 — Key equations

1. Master geodesic-deviation equation:
$$\ddot{\xi}^i = \tfrac{1}{2}\, \ddot{h}_{ij}^{\rm TT}\, \xi^j .$$
2. Proper-distance change:
$$\frac{\Delta s}{L} = \tfrac{1}{2}\, h_{ij}^{\rm TT}\, \hat{n}^i \hat{n}^j .$$
3. Newtonian tidal force:
$$F^i = \tfrac{m}{2}\, \ddot{h}_{ij}^{\rm TT}\, \xi^j .$$
4. Light round-trip correction (TT):
$$t_{\rm rt}(t_0) - 2L/c = \frac{L\, h_0}{c}\, \mathrm{sinc}\!\left(\tfrac{\omega_{\rm gw} L}{c}\right)\, \cos\left[\omega_{\rm gw}(t_0 + L/c)\right].$$
5. Detector output:
$$h(t) = F_+(\theta,\phi,\psi)\, h_+(t) + F_\times(\theta,\phi,\psi)\, h_\times(t).$$

Order-of-magnitude anchor. For $h{\sim}10^{-21}$ and $L{\sim}3$ km, $\Delta L{\sim}3\times10^{-18}$ m.

Block 1 — Further reading

[1] Michele Maggiore. *Gravitational Waves. Vol. 1: Theory and Experiments*. Oxford: Oxford University Press, 2007. ISBN: 978-0-19-857074-5. DOI: 10.1093/acprof:oso/9780198570745.001.0001.

[2] Jolien D. E. Creighton and Warren G. Anderson. *Gravitational-Wave Physics and Astronomy: An Introduction to Theory, Experiment and Data Analysis*. Weinheim: Wiley-VCH, 2011. ISBN: 978-3-527-40886-3. DOI: 10.1002/9783527636037.

[3] Peter R. Saulson. *Fundamentals of Interferometric Gravitational Wave Detectors*. 2nd ed. Singapore: World Scientific, 2017. ISBN: 978-981-314-307-4. DOI: 10.1142/9book.

[4] Éanna É. Flanagan and Scott A. Hughes. "The basics of gravitational wave theory". In: *New Journal of Physics* 7 (2005), p. 204. DOI: 10.1088/1367-2630/7/1/204. arXiv: gr-qc/0501041.

Block 1 — Exercises

1. **Christoffel in TT gauge.** Starting from $\Gamma^{\mu}_{\alpha\beta} = \frac{1}{2}\, g^{\mu\nu}\,(\partial_\alpha g_{\nu\beta} + \partial_\beta g_{\nu\alpha} - \partial_\nu g_{\alpha\beta})$, compute to first order in h the components Γ^{i}_{00}, Γ^{0}_{ij} and Γ^{i}_{0j} in TT gauge. Verify equation (1.17) explicitly, and show that $\Gamma^{0}_{ij} = (1/2c)\,\dot{h}^{\rm TT}_{ij}$ and $\Gamma^{i}_{0j} = (1/2c)\,\dot{h}^{\rm TT}_{ij}$.

2. **Proper distance for an arbitrary arm direction.** Take a wave travelling along $\hat{z}$ with arbitrary polarization amplitudes h_+ and $h_\times$. Consider two free test masses separated along the direction $\hat{n} = (\sin\theta\cos\phi, \sin\theta\sin\phi, \cos\theta)$ by coordinate distance L. Show that the fractional proper-distance change is

$$\frac{\Delta s}{L} = \tfrac{1}{2}\big[h_+\,(\sin^2\theta\cos 2\phi) + h_\times\,(\sin^2\theta\sin 2\phi)\big].$$

   For a detector whose arm is horizontal ($\theta = \pi/2$) with a wave from zenith ($\hat{k} = \hat{z}$), recover the expected quadrupolar dependence on ϕ.

3. **Sinc factor: one-way vs round-trip.** Starting from the one-way result (1.30), derive the round-trip result (1.33). Identify the steps where (i) the forward and return contributions combine, (ii) the argument of the sinc doubles from $\omega_{\rm gw}L/(2c)$ to $\omega_{\rm gw}L/c$. Show that in the long-wavelength limit both give $\Delta t_{\rm rt} \simeq h\,L/c$ and $\Delta t_{\text{one-way}} \simeq h\,L/(2c)$.

4. **Antenna pattern at a specific configuration.** Consider a detector at the Earth's equator with arms pointing east and north.

   (a) For a source directly overhead (zenith direction) and polarization angle $\psi = 0$, evaluate F_+ and $F_\times$. Compare with the value at $\psi = \pi/4$ to confirm that $F_+^2 + F_\times^2$ is independent of ψ.

   (b) For a source at the horizon, due east, evaluate F_+ and $F_\times$. Interpret the result physically.

   (c) Compute $F_+^2 + F_\times^2$ as a function of θ averaged over ϕ and ψ, and verify that the result is $(1 + 6\cos^2\theta + \cos^4\theta)/10$. The average over the full sky of this quantity is $2/5$: the detector, over a sidereal day, has an rms directional sensitivity of $\sqrt{2/5} \simeq 0.63$.

5. **Ring deformation under a general polarization.** Let a GW propagating along $\hat{z}$ have polarization amplitudes $h_+(t) = h_0\cos(\omega_{\rm gw}t)$ and $h_\times(t) = h_0\cos(\omega_{\rm gw}t + \delta)$, with δ the relative phase. Show that the ring of test masses is deformed into an ellipse whose axes rotate in time for $\delta \neq 0, \pi$, and that the special case $\delta = \pi/2$ with equal amplitudes gives a *circularly-polarized* wave: the ellipse axes rotate at the GW frequency while the ellipse shape is constant.

Chapter 2

Block 2 — Experimental Fundamentals

Block overview

Block 2 is experimental. It asks how an optical instrument turns the differential length change produced by a gravitational wave into a voltage on a photodiode, and what stands between the ideal response and the noise floor of a real detector.

The material is organised in four sections:

- **Section 2.1.** From theory to instrument. Scale of the problem, Michelson basics, shot-noise-limited sensitivity.
- **Section 2.2.** Why real detectors are not plain Michelsons. Fabry–Perot arm cavities, power recycling, signal recycling, squeezing.
- **Section 2.3.** Noise budget. Seismic, Newtonian, thermal, quantum. How to read a real sensitivity curve.
- **Section 2.4.** Network, reach, and the horizon for third-generation detectors.

By the end of Block 2 a student should be able to:

- write down the shot-noise-limited strain sensitivity of a simple Michelson and state its numerical value for km-scale arms;
- explain the physical role of Fabry–Perot arm cavities, power recycling, signal recycling, and squeezing, and give the associated gain factors;
- identify the dominant noise source in each decade of the sensitivity curve of an advanced ground-based detector;
- apply the fluctuation–dissipation theorem to the pendulum mode of a suspended test mass with the correct dimensional prefactor;
- derive the Standard Quantum Limit from the competition between shot noise and radiation-pressure noise;
- relate strain sensitivity to BNS range and explain why sky localisation requires a network.

2.1 From theory to instrument

Block 1 produced a clean definition of the detector output:

$$h(t) \;=\; F_+(\theta,\phi,\psi)\,h_+(t) \;+\; F_\times(\theta,\phi,\psi)\,h_\times(t),$$

and a linear optical response of a single arm: audio sidebands at $\omega_L \pm \omega_{\rm gw}$ with amplitude proportional to $h_0\,k_L L\,\mathrm{sinc}(\omega_{\rm gw}L/c)$ around the laser carrier. This section closes the gap between that response and a voltage on a photodiode, and computes the sensitivity of the simplest instrument that does the job.

2.1.1 Recap from Block 1 and the core question

The quantity the instrument must measure is the differential arm-length change normalised to the arm length,

$$h(t) \;=\; \frac{\Delta L_x(t) - \Delta L_y(t)}{L}. \tag{2.1}$$

For a compact binary coalescence at a distance of order 100 Mpc, the peak strain is $h{\sim}10^{-21}$. For arm lengths of a few km this translates into

$$\Delta L \;\sim\; h\,L \;\sim\; 3\times10^{-18}\ \text{m}.$$

To reach this level with usable signal-to-noise ratio across the detection band, the target amplitude spectral density of the strain output is

$$\sqrt{S_h(f)} \;\sim\; 10^{-23}\ \text{Hz}^{-1/2} \qquad \text{between 10 Hz and 10 kHz.} \tag{2.2}$$

The core question of Block 2. How do we build an instrument with strain sensitivity $\sqrt{S_h(f)}{\sim}10^{-23}$ Hz$^{-1/2}$ in the band 10 Hz to 10 kHz? Every noise source discussed in Sections 2.2 and 2.3 is a competing effect that limits our ability to reach this number.

2.1.2 The scale of the problem

The number $\Delta L{\sim}10^{-18}$ m has no counterpart in everyday experimental physics. A compact table of length scales gives the right sense of the challenge.

Numerical check. *Lengths of interest.*

- Laser wavelength, $\lambda_L = 1064$ nm: 1.064×10^{-6} m.
- Atomic radius (hydrogen Bohr radius): 5.3×10^{-11} m.
- Nuclear radius, medium nucleus: $\sim5\times10^{-15}$ m.
- Proton charge radius: 0.84×10^{-15} m.
- Differential arm-length change from a BNS merger at 100 Mpc, $L = 3$ km: $\sim3\times10^{-18}$ m.

The target is three orders of magnitude smaller than a proton, and twelve orders of magnitude smaller than the laser wavelength.

This is the measurement goal. The remainder of Block 2 is a catalogue of the obstacles between us and this number, and the techniques used to get around them.

2.1.3 Why interferometry, why differential

Two experimental choices are dictated by the numbers.

Interferometry converts length into phase. A length change ΔL along a light path produces a phase shift

$$\Delta\varphi \;=\; k_L\,\Delta L \;=\; \frac{2\pi\,\Delta L}{\lambda_L}. \tag{2.3}$$

For $\lambda_L = 1064$ nm and $\Delta L = 10^{-18}$ m this gives $\Delta\varphi{\sim}6\times10^{-12}$ rad. A phase this small is measurable: photon-counting statistics on a photodiode reading a bright field set a shot-noise floor of order $\Delta\varphi_{\text{shot}}{\sim}1/\sqrt{N_{\text{ph}}}$, which falls below 10^{-11} rad/$\sqrt{\text{Hz}}$ for optical power of order a watt.

Differential measurement doubles the signal and rejects common-mode noise. In the long-wavelength limit (Section 1.2), a +-polarised wave propagating along $\hat{z}$ and passing through a detector with arms along $\hat{x}$ and $\hat{y}$ produces $\Delta L_x/L = (1/2)\,h_+$ and $\Delta L_y/L = -(1/2)\,h_+$. The differential combination $\Delta L_x - \Delta L_y = L\,h_+$ doubles the single-arm response. The same combination also rejects any disturbance that acts symmetrically on the two arms: laser frequency fluctuations, temperature drifts of common optics, and vibration modes that translate the whole apparatus rigidly.

A Michelson interferometer is the simplest optical topology that implements both ideas at once: a beam splitter divides the light into two orthogonal arms, each arm terminates on a mirror acting as a test mass, and the recombined beams are read out on a photodiode. This is the starting point for every ground-based GW detector.

2.1.4 Michelson topology and dark-fringe operation

Label the laser field at the input of the beam splitter $E_0\,\mathrm{e}^{-i\omega_L t}$, with E_0 real. A symmetric 50/50 beam splitter produces two equal-amplitude beams propagating into the x and y arms, each of length L. After reflection on the end mirrors and return to the beam splitter, the two beams acquire phases $2k_L L_x$ and $2k_L L_y$ respectively. Recombining them at the beam splitter produces an output field at the asymmetric ("dark") port,

$$E_{\mathrm{out}} \;=\; \tfrac{1}{2}\,E_0\left[\mathrm{e}^{2ik_L L_x} - \mathrm{e}^{2ik_L L_y}\right]\mathrm{e}^{-i\omega_L t}. \tag{2.4}$$

The output power is

$$P_{\mathrm{out}} \;=\; |E_{\mathrm{out}}|^2 \;=\; \tfrac{1}{2}\,P_{\mathrm{in}}\left[1 - \cos\big(2k_L(L_x - L_y)\big)\right] \;=\; P_{\mathrm{in}}\,\sin^2\!\big(k_L(L_x - L_y)\big), \tag{2.5}$$

which is the familiar fringe curve. The response of the output power to an arm-length difference $\Delta L \equiv L_x - L_y$ has the form

$$\frac{\mathrm{d}P_{\mathrm{out}}}{\mathrm{d}\Delta L} \;=\; k_L\,P_{\mathrm{in}}\,\sin\!\big(2k_L\,\Delta L\big).$$

Pitfall. The slope of the fringe, and therefore the response to a length change, *vanishes* at the top of the fringe ($\Delta L = \lambda_L/4$) and at the dark port ($\Delta L = 0$). Running the Michelson exactly at the dark port gives zero DC sensitivity, the opposite of what is wanted. The apparent paradox is resolved below: in practice, the output field carries a small carrier (either an intentional DC offset or radio-frequency sidebands) that provides a local oscillator against which the signal sidebands beat. It is the beat, not the DC power, that carries the signal.

Two independent reasons motivate running close to the dark port, not at a mid-fringe point:

- **Laser intensity noise.** At mid-fringe, any relative intensity fluctuation $\delta P/P$ of the laser appears directly in the output. At the dark port, the intensity coupling vanishes to first order because $P_{\mathrm{out}} \to 0$.
- **Scattered and thermal light.** A dark output has minimal steady-state power on the photodiode; shot noise on a bright background would otherwise dominate.

The cost of dark-fringe operation is the need for an active readout scheme (DC readout with a small offset, or heterodyne readout via RF sidebands) that is discussed briefly below and in detail in the dedicated control lecture of the school (D. Bersanetti, Sat 23).

2.1.5 The output field in the presence of a GW

To first order in the strain, $L_x(t) = L + \delta L_x(t)$ and $L_y(t) = L + \delta L_y(t)$, with $\delta L_x - \delta L_y = L\,h(t)$. Expanding (2.4) around the mean length L and keeping first order in h:

Derivation.
Write $L_x = L + \frac{1}{2}Lh(t)$, $L_y = L - \frac{1}{2}Lh(t)$, where the factor $\frac{1}{2}$ follows from $\Delta L_x - \Delta L_y = Lh$ together with the assumption of equal arms at rest. Substituting into (2.4),

$$\begin{aligned} E_{\rm out}(t) &= \tfrac{1}{2}\,E_0\,\mathrm{e}^{2ik_L L}\left[\mathrm{e}^{+ik_L L\,h(t)} - \mathrm{e}^{-ik_L L\,h(t)}\right]\mathrm{e}^{-i\omega_L t} \\ &\simeq i\,E_0\,\mathrm{e}^{2ik_L L}\,k_L L\,h(t)\,\mathrm{e}^{-i\omega_L t}. \end{aligned}$$

The factor $\mathrm{e}^{2ik_L L}$ is a static common phase. The key feature is the linear dependence on $h(t)$, with prefactor $k_L L$. For a monochromatic GW at angular frequency $\omega_{\rm gw}$, $h(t) = h_0\cos(\omega_{\rm gw} t)$, so the output acquires sidebands at $\omega_L \pm \omega_{\rm gw}$ with amplitude $(1/2)\,E_0\,k_L L\,h_0$. A finite light-travel time $2L/c$ across the arm multiplies this amplitude by $\mathrm{sinc}(\omega_{\rm gw} L/c)$, recovering the result of Section 1.2 from the Michelson output directly.

On a photodiode the output power is $P_{\rm out}(t) = |E_{\rm out}|^2$, which vanishes at the dark port to first order in h. A non-zero first-order photocurrent requires a local oscillator. Two standard options:

- **DC readout.** A small, controlled offset is added to ΔL, so that a static carrier $E_{\rm LO} \propto E_0\,\Delta L_{\rm off}$ reaches the photodiode. The beat between $E_{\rm LO}$ and the signal sidebands produces a photocurrent linear in $h(t)$.

- **Heterodyne readout.** Radio-frequency sidebands are imprinted on the laser (by phase modulation) and tuned so that they reach the photodiode. The demodulated output at the modulation frequency is again linear in $h(t)$.

Both schemes are in use in advanced detectors. Advanced Virgo and Advanced LIGO operate in DC readout; heterodyne variants are used for auxiliary length and alignment sensing. The full treatment is in the controls lecture of this school (D. Bersanetti, Sat 23).

2.1.6 From phase to strain, and the sinc factor

Collecting the results above, the GW-induced phase shift at the output of a simple Michelson, at GW frequency $f_{\rm gw}$ and with equal arms of length L, is

$$\boxed{\Delta\varphi_{\rm gw}(f_{\rm gw}) \;=\; \frac{4\pi L}{\lambda_L}\,h\,\mathrm{sinc}\!\left(\frac{2\pi f_{\rm gw} L}{c}\right).} \tag{2.6}$$

The factor $4\pi L/\lambda_L$ expresses the phase accumulation on the round trip in *both* arms and includes the differential-measurement factor of two. The sinc factor is the same frequency response derived from first principles in Block 1. For a 3 km arm and $f_{\rm gw} \lesssim 10$ kHz, $\mathrm{sinc}(\omega_{\rm gw} L/c) \simeq 1$ and the response is essentially flat in frequency.

Note. The sinc response rolls off on a frequency scale $f_{\rm gw} \sim c/(2L)$. For $L = 3$ km, $c/(2L) \simeq 50$ kHz, well above the advanced-detector band. For Einstein Telescope ($L \simeq 10$ km), the roll-off frequency is $\sim$15 kHz. The Michelson response is flat throughout the ground-based detection band.

2.1.7 Shot-noise-limited Michelson: the benchmark number

The quantum statistics of the detected photons set a floor on the smallest measurable phase. For a Poisson-distributed photon number N_{ph} collected in a time τ,

$$\Delta\varphi_{\mathrm{shot}} \simeq \frac{1}{\sqrt{N_{\mathrm{ph}}}}, \qquad N_{\mathrm{ph}} = \frac{P_{\mathrm{in}}\,\tau}{\hbar\omega_L}. \tag{2.7}$$

Expressed as an amplitude spectral density over a $1/(2\tau)$ bandwidth (standard single-sided convention),

$$\sqrt{S_\varphi^{\mathrm{shot}}(f)} = \sqrt{\frac{\hbar\omega_L}{P_{\mathrm{in}}}} \qquad [\mathrm{rad}/\sqrt{\mathrm{Hz}}]. \tag{2.8}$$

Derivation.

Inverting (2.6) in the limit of unit sinc gives $h = (\lambda_L/(4\pi L))\,\Delta\varphi_{\mathrm{gw}}$. Dividing by the shot-noise-limited phase (2.8) produces the amplitude spectral density of the equivalent strain at the output:

$$\sqrt{S_h^{\mathrm{shot}}(f)} = \frac{\lambda_L}{4\pi L}\sqrt{\frac{\hbar\omega_L}{P_{\mathrm{in}}}} = \frac{1}{L}\sqrt{\frac{\hbar c\lambda_L}{4\pi P_{\mathrm{in}}}}. \tag{2.9}$$

The prefactor of $1/L$ is the reason arm length matters; the $P_{\mathrm{in}}^{-1/2}$ scaling is the reason circulating power matters.

Numerical check. *Benchmark.* Take $L = 3$ km, $\lambda_L = 1064$ nm, $\omega_L = 2\pi c/\lambda_L \simeq 1.77\times10^{15}$ rad/s, $P_{\mathrm{in}} = 10$ W.

$$\sqrt{S_\varphi^{\mathrm{shot}}} = \sqrt{\frac{1.05\times10^{-34}\,\mathrm{J\,s}\cdot 1.77\times10^{15}\,\mathrm{rad/s}}{10\,\mathrm{W}}} \simeq 1.4\times10^{-10}\ \mathrm{rad}/\sqrt{\mathrm{Hz}}.$$

$$\sqrt{S_h^{\mathrm{shot}}} = \frac{\lambda_L}{4\pi L}\sqrt{S_\varphi^{\mathrm{shot}}} \simeq \frac{1.064\times10^{-6}}{4\pi\cdot 3\times10^{3}}\cdot 1.4\times10^{-10} \simeq 4\times10^{-21}\ \mathrm{Hz}^{-1/2}.$$

A simple Michelson with 10 W of input power and km-scale arms sits at $\sim10^{-20}/\sqrt{\mathrm{Hz}}$, two to three orders of magnitude above the target (2.2).

Take-away. A bare Michelson with reasonable laser power is off the target by 10^2 to 10^3. Closing this gap is the subject of Section 2.2. The three levers are: longer effective path, higher circulating power, and a lower noise floor than the vacuum itself.

2.2 Why real detectors are not plain Michelsons

The shot-noise formula (2.9) shows two independent handles for improving sensitivity:

$$\sqrt{S_h^{\mathrm{shot}}} \propto \frac{1}{L\sqrt{P_{\mathrm{in}}}}.$$

Arm length is set by site engineering and can be pushed only so far: Advanced LIGO and Advanced Virgo use $L = 4$ km and 3 km respectively. Einstein Telescope targets $L = 10$ km underground. Between these hard limits and the target (2.2), the remaining gain comes from optical configurations that enhance the phase response at fixed arm length or increase the circulating power at fixed laser power. The four techniques discussed below are present in every advanced detector.

2.2.1 Two handles: longer effective path, more photons

A first reading of $\sqrt{S_h^{\rm shot}} \propto 1/(L\sqrt{P_{\rm in}})$ suggests pushing both variables as far as possible. The trade-offs are:

- **Arm length.** Civil-engineering and vacuum-system costs grow faster than linear with L. The sinc factor rolls off at $f{\sim}c/(2L)$, which constrains the maximum useful arm length at the high-frequency end of the band. For ground-based detectors this is not yet a limitation.
- **Laser power.** High-power stabilised lasers are a mature technology; advanced detectors use ∼50–150 W input lasers. Circulating power in the arms is a different story: mirror absorption and thermal lensing cap the useful value well below what the laser alone would provide.

Both hard limits are addressed by resonant optical cavities. A Fabry–Perot cavity in each arm extends the effective light path at fixed geometric arm length; a power-recycling cavity folds the carrier back into the interferometer and increases the circulating power at fixed laser power. A third cavity, the signal-recycling cavity, reshapes the frequency response to the GW signal. Each of these is discussed in detail in dedicated school lectures (A. Perreca, Fri 22 & Sat 23; D. Bersanetti, Sat 23); the notes here give the essential gain factors and the one derivation that fits in a paragraph (the FP cavity pole).

2.2.2 Fabry–Perot arm cavities

An arm Fabry–Perot (FP) cavity is a high-finesse optical resonator formed between the input test mass (ITM) and the end test mass (ETM). Light injected through the partially transmitting ITM builds up inside the cavity; at resonance, the stored power is larger than the incident power by a factor $\sim 2\mathcal{F}/\pi$, where $\mathcal{F}$ is the cavity finesse.

For sensitivity to GWs, the relevant quantity is not the stored power but the *effective light path*. At resonance, a photon makes on average $\mathcal{N} = 2\mathcal{F}/\pi$ round trips before leaking out, so the effective arm length is

$$L_{\rm eff} \;\simeq\; \mathcal{N}\, L \;=\; \frac{2\mathcal{F}}{\pi}\, L. \tag{2.10}$$

For Advanced Virgo, $\mathcal{F} \simeq 450$ and $L = 3$ km give $L_{\rm eff} \simeq 860$ km. The phase response (2.6) is enhanced by the same factor at low GW frequencies, bringing the shot-noise-limited strain sensitivity down by $L_{\rm eff}/L = 2\mathcal{F}/\pi$.

The enhancement does not extend to arbitrarily high GW frequencies. The photon storage time $\tau_{\rm s} = L_{\rm eff}/c$ sets a cavity pole above which the response rolls off as $1/f$.

Derivation.

Model the FP cavity as a single-pole low-pass filter for the GW signal. The input is a length change $\delta L(t)$ of the cavity; the output is the accumulated phase shift of the circulating field. At GW frequency f, a photon entering the cavity experiences the full $\mathcal{N}$ bounces only if the signal persists for longer than the storage time. For signals faster than $1/\tau_{\rm s}$, the effective number of bounces is reduced. The transfer function from length change to phase response has the form

$$H(f) \;=\; \frac{2k_L\, L_{\rm eff}}{1 + i\, f/f_{\rm pole}},$$

with cavity pole

$$\boxed{f_{\rm pole} \;=\; \frac{1}{4\pi\tau_{\rm s}} \;=\; \frac{c}{4\,\mathcal{F}\,L}.} \tag{2.11}$$

Numerical check. *Advanced Virgo.* $\mathcal{F} \simeq 450$, $L = 3$ km give $f_{\rm pole} \simeq c/(4 \cdot 450 \cdot 3000)$ Hz $\simeq 56$ Hz. *Advanced LIGO.* $\mathcal{F} \simeq 450$, $L = 4$ km give $f_{\rm pole} \simeq 42$ Hz. *Einstein Telescope* (high-frequency interferometer, design). $\mathcal{F} \simeq 900$, $L = 10$ km give $f_{\rm pole} \simeq 8$ Hz. Above the pole, the shot-noise-limited strain has an additional factor $\sqrt{1 + (f/f_{\rm pole})^2}$; below the pole, the FP gain is flat.

Pitfall. The phase response of an FP cavity is enhanced at low frequency, but *radiation-pressure* noise (Section 2.3.10) is enhanced by the same factor. The FP cavity boosts the signal and the back-action-limited noise by the same amount, leaving the signal-to-noise ratio unchanged at the Standard Quantum Limit. What FP buys is a shift of the quantum noise spectrum to match the rest of the noise budget, together with a large gain against technical noises on the beam splitter.

2.2.3 Power recycling

A dark-fringe Michelson reflects essentially all of the carrier light back toward the laser. A partially transmitting mirror (the power-recycling mirror, PRM) placed between the laser and the beam splitter forms a new cavity, the power-recycling cavity (PRC), with the bright side of the Michelson as its back mirror. When the PRC is held on resonance for the carrier, the circulating carrier power inside the interferometer is enhanced by a recycling gain

$$G_{\rm PR} = \frac{1}{(1 - r_{\rm PRM}\sqrt{1 - \ell_{\rm rt}})^2}, \tag{2.12}$$

where $r_{\rm PRM}$ is the amplitude reflectivity of the PRM and $\ell_{\rm rt}$ is the total round-trip power loss inside the interferometer (mirror absorption, scatter, imperfect contrast at the beam splitter).

In Advanced Virgo and Advanced LIGO, $G_{\rm PR} \simeq 30$–40, bringing the arm-cavity circulating power from ∼10 kW to ∼400 kW with an input laser of ∼50–150 W. The impact on shot-noise-limited strain sensitivity is a factor $\sqrt{G_{\rm PR}} \simeq 6$ reduction.

Note. The recycling gain is set by the losses in the interferometer: the higher the reflectivity of the PRM, the larger $G_{\rm PR}$, but also the narrower the PRC resonance and the more sensitive the instrument becomes to mismatch and drifts. In practice, $r_{\rm PRM}$ is chosen so that the PRC is critically coupled to the losses, which maximises the circulating power for a given level of technical imperfection.

2.2.4 Signal recycling

A second partially transmitting mirror (the signal-recycling mirror, SRM) is placed at the output port, between the beam splitter and the photodiode. The SRM forms yet another cavity, the signal-recycling cavity (SRC), with the dark side of the Michelson as its back mirror. The GW-induced signal sidebands see this cavity and are either resonantly enhanced (tuned signal recycling) or frequency-shifted (detuned signal recycling).

The effect on the strain sensitivity curve is a reshaping, not a uniform gain:

- **Tuned SR** narrows the bucket of the sensitivity curve around an adjustable resonance, exchanging bandwidth for peak sensitivity. Useful for targeted searches.
- **Detuned SR** introduces a sharp resonance below the arm-cavity pole, recovering low-frequency sensitivity at the cost of response above the resonance.

Dual-recycled, FP Michelson is the baseline topology of every advanced GW interferometer. A schematic is covered in the dedicated optical-configurations lecture of this school.

2.2.5 Squeezing

Shot noise and radiation-pressure noise both originate from vacuum fluctuations of the optical field entering the interferometer through the dark port. The vacuum amplitude and phase quadratures satisfy an uncertainty relation $\Delta X_1 \, \Delta X_2 \geq 1/2$ (in appropriate normalisation). *Squeezed vacuum* is a non-classical state for which one quadrature has $\Delta X < 1/2$, at the price of the conjugate quadrature having $\Delta X > 1/2$.

Injecting squeezed vacuum through the dark port reduces the noise quadrature relevant for the readout. The improvement factor on the amplitude spectral density is

$$r_{\mathrm{sq}} \;=\; \mathrm{e}^{-r}, \tag{2.13}$$

where r is the squeezing parameter. A squeezing level of 6 dB in power corresponds to $r = \ln(10^{0.6})/2 \simeq 0.69$ and $r_{\mathrm{sq}} \simeq 0.5$, a factor-two reduction of the noise floor in amplitude. Optical losses degrade this: a squeezer producing 10 dB at the source delivers ∼3–4 dB at the readout after passage through the interferometer, depending on losses.

Two regimes:

- **Frequency-independent squeezing** rotates the squeezing ellipse at a fixed angle. It reduces either shot noise or radiation-pressure noise, not both. Used in advanced detectors from O3 onward, tuned to reduce shot noise at high frequency.
- **Frequency-dependent squeezing** uses a filter cavity to rotate the squeezing angle as a function of frequency, so that shot noise is reduced above a crossover frequency and radiation-pressure noise is reduced below it. Deployed in the LIGO–Virgo network in O4 and baseline for third-generation detectors.

Note. Historical anchors worth remembering in the lecture: Caves 1981 (vacuum origin of quantum noise); GEO600 (first long-term squeezing in a GW detector, 2010s); aLIGO H1 demonstration (2019), published as Tse et al., PRL 123, 231107; frequency-independent squeezing operational in Advanced Virgo and Advanced LIGO in O4.

2.3 Noise budget — the fundamentals

The instrument described in Sections 2.1 and 2.2 is an ideal transducer from strain to photocurrent. A real detector is limited by a zoology of noises that enter the readout at every frequency. This section covers the fundamental ones (seismic, Newtonian, thermal, quantum) at the level of dimensional estimates and scaling laws, and ends with a walk-through of a real advanced-detector noise budget.

2.3.1 Two design principles

Hild's compact statement of the design problem, adapted from [1], frames the entire section:

1. The test masses must be **quieter than the signal** to be observed.
2. The test-mass position must be **read out with adequate accuracy**, without introducing unacceptable back-action.

Principle 1 drives the **mechanical** design: suspensions, seismic isolation, low-loss coatings, vacuum, site selection. Principle 2 drives the **optical** design: high circulating power, dark-fringe operation, readout scheme, squeezing, quantum-non-demolition techniques.

Every noise source discussed below falls into one of the two categories. Displacement noises (seismic, Newtonian, thermal) belong to category 1; readout noises (shot noise, laser frequency and intensity noise, photodiode electronics) and back-action noise (radiation pressure) belong to category 2.

2.3.2 The sensitivity curve as a map of the detector

The single figure of merit of a GW detector is the amplitude spectral density of the equivalent strain output,

$$\sqrt{S_h(f)} \qquad [\mathrm{Hz}^{-1/2}].$$

Every displacement noise with amplitude spectral density $\sqrt{S_x^{(i)}(f)}$ on a mirror translates into a strain-equivalent noise $\sqrt{S_h^{(i)}(f)} = \sqrt{S_x^{(i)}(f)}\,/L$, where L is the arm length (not L_{eff}; the Fabry–Perot gain cancels between signal and displacement noise on the test mass).

A typical advanced-detector sensitivity curve has three regions, each dominated by a different physics driver:

- **Low frequency** ($\lesssim 30$ Hz): a steep wall set by seismic and Newtonian noise, together with the low-frequency tails of suspension thermal noise.
- **Mid frequency** (30 Hz to 300 Hz): the bucket of the curve, set by coating thermal noise and, at the very low end, by radiation-pressure noise.
- **High frequency** ($\gtrsim 300$ Hz): an approximately flat or slowly rising floor set by shot noise, modulated by the arm-cavity pole and by signal recycling.

Each feature of the curve maps back onto a component of the instrument. Reading the curve is an exercise in identifying which noise contribution is responsible for which region, and deciding where to invest effort for the next upgrade.

2.3.3 Seismic noise

The ground is never at rest. Even at a quiet site, displacement amplitudes of the Earth surface in the GW detection band have the approximate form

$$\sqrt{S_x^{\mathrm{seis}}(f)} \;\simeq\; A \cdot \left(\frac{1\ \mathrm{Hz}}{f}\right)^{\nu} \qquad [\mathrm{m}/\sqrt{\mathrm{Hz}}], \tag{2.14}$$

with $A{\sim}10^{-7}$ m/$\sqrt{\mathrm{Hz}}$ and $\nu \simeq 2$ above $\sim$1 Hz for a typical surface site. The amplitude and the slope depend strongly on the local environment: Cascina and Livingston are noisier than Hanford; underground sites (Kamioka, Sos Enattos) are quieter still, which motivates the Einstein Telescope design.

Numerical check. *Order of magnitude at 10 Hz.* At a typical surface site, the seismic amplitude spectral density at 10 Hz is $\sim 10^{-9}$ m/$\sqrt{\mathrm{Hz}}$. Unattenuated, this converts to a strain noise $\sim 10^{-9}/3000\,\mathrm{m} \sim 3 \times 10^{-13}$ Hz$^{-1/2}$, ten orders of magnitude above the target. Seismic isolation must provide at least 10 orders of magnitude of attenuation at 10 Hz.

A characteristic feature of the spectrum is the **microseism peak** between 0.1 and 0.3 Hz, produced by ocean swell. The peak is mostly below the detection band, but its amplitude (of order 10^{-6} m/$\sqrt{\mathrm{Hz}}$) drives the dynamic range of the seismic isolation system and the payload of the active platforms.

2.3.4 Seismic isolation

Seismic isolation relies on the transfer function of a cascade of mechanical resonators. A single pendulum of resonant frequency f_0, driven at frequency $f \gg f_0$, transmits ground motion to the suspended mass attenuated by

$$\left|\frac{x_{\mathrm{mass}}}{x_{\mathrm{ground}}}\right| \;\simeq\; \left(\frac{f_0}{f}\right)^2. \tag{2.15}$$

For $f_0 \simeq 0.5$ Hz and $f = 10$ Hz, a single pendulum attenuates by a factor $(0.5/10)^2 = 2.5 \times 10^{-3}$. Achieving the required $\sim 10^{-10}$ at 10 Hz needs a multi-stage suspension. The Virgo **superattenuator** is a six-stage compound pendulum with an overall attenuation better than 10^{-12} above a few Hz, below the internal resonances of the chain. The Advanced LIGO quadruple pendulum provides $\sim 10^{-7}$ attenuation at 10 Hz, with the remaining orders supplied by active platforms.

Note. Vertical-to-horizontal coupling matters. A pendulum isolates in the direction of its axis; cross-couplings at the percent level mean that vertical ground motion, which is not isolated by the simple pendulum, can leak into horizontal motion of the test mass. The superattenuator includes vertical-blade filters with a blade-spring resonant frequency of ~ 0.4 Hz to attenuate vertical motion as well.

2.3.5 Newtonian (gravity-gradient) noise

Fluctuations in the local Newtonian gravitational field, produced by density variations around the detector, accelerate the test mass directly through its gravitational mass. This noise cannot be attenuated by any mechanical suspension, because the perturbation is gravitational and acts on every test mass in the same way.

The dominant contribution is from seismic Rayleigh waves passing near the detector: the pressure wave compresses the rock asymmetrically on the two sides of the test mass, producing a net force. The order of magnitude of the strain noise from Newtonian gravity-gradient is, for a surface detector,

$$\sqrt{S_h^{\mathrm{NN}}(f)} \;\sim\; \frac{G\rho}{f^2}\,\beta(f)\,\sqrt{S_x^{\mathrm{seis}}(f)},$$

where ρ is the local soil density and $\beta(f)$ is a transfer function of order unity. At 10 Hz and for a surface site, this sits a factor few below advanced-detector seismic noise, but above the target for third-generation detectors.

Note. Newtonian noise is the primary driver of the Einstein Telescope underground choice. At depths $\gtrsim 100$ m the surface-wave contribution to gravity-gradient noise is strongly suppressed. Active cancellation schemes, based on seismometer arrays around the test masses, are an active R&D topic and are expected to provide residual suppression in both current and future detectors.

2.3.6 Thermal noise — the fluctuation–dissipation theorem

Any mechanical degree of freedom coupled to a thermal bath has fluctuating position, with spectrum set by the dissipation. The fluctuation–dissipation theorem (FDT, Callen and Welton 1951) relates the spectrum of position fluctuations to the imaginary part of the mechanical admittance $Y(\omega) = -i\omega\,\alpha(\omega)$, where $\alpha(\omega)$ is the complex response function:

$$S_x(\omega) \;=\; -\frac{4k_B T}{\omega}\,\mathrm{Im}\,\alpha(\omega). \tag{2.16}$$

Derivation.

Apply (2.16) to a damped harmonic oscillator with equation of motion

$$m\ddot{x} + \gamma\dot{x} + \kappa\,x \;=\; f(t), \qquad \omega_0^2 = \kappa/m, \qquad Q = m\omega_0/\gamma.$$

In the frequency domain,

$$\alpha(\omega) \;=\; \frac{1}{\kappa - m\omega^2 + i\omega\gamma}, \qquad \mathrm{Im}\,\alpha(\omega) \;=\; \frac{-\omega\gamma}{(\kappa - m\omega^2)^2 + (\omega\gamma)^2}.$$

Substituting into (2.16) and using $\gamma = m\omega_0/Q$ gives the displacement spectrum in the viscous-damping approximation:

$$\boxed{S_x(\omega) \;=\; \frac{4k_B T\,\omega_0/Q}{m\left[(\omega^2 - \omega_0^2)^2 + (\omega\,\omega_0/Q)^2\right]}.} \tag{2.17}$$

Two limits of (2.17) are useful:

- **Below the resonance** ($\omega \ll \omega_0$): $S_x(\omega) \simeq 4k_B T\,\omega_0/(Q\,m\,\omega_0^4) = 4k_B T/(Q\,m\,\omega_0^3)$, flat in frequency.
- **Above the resonance** ($\omega \gg \omega_0$): $S_x(\omega) \simeq 4k_B T\,\omega_0/(Q\,m\,\omega^4)$, falling as $1/\omega^4$.

Most of the thermal-noise budget of a GW detector falls in the above-resonance regime: the pendulum mode is at ∼0.5 Hz and the detection band starts at ∼10 Hz. The violin modes of the suspension wires, at ∼500 Hz and harmonics, appear as sharp peaks in the bucket of the sensitivity curve.

2.3.7 Suspension thermal noise

The last stage of the test-mass suspension is the main source of low-frequency thermal noise. In Advanced Virgo and Advanced LIGO, the test masses are suspended by thin fibres (fused silica, ∼0.4 mm diameter for AdV) that form a monolithic stage at the bottom of the superattenuator or quadruple pendulum.

The thermal-noise amplitude on the pendulum mode is reduced relative to a bulk oscillator by a **dilution factor**

$$D \;=\; \frac{E_{\mathrm{grav}}}{E_{\mathrm{elast}}} \;\gg\; 1, \tag{2.18}$$

where E_{grav} is the gravitational restoring energy of the pendulum and E_{elast} is the elastic energy stored in the suspension fibres. Most of the restoring force in a long pendulum comes from gravity; only a small fraction comes from the elastic bending of the fibres. Since the dissipation is carried by the elastic part, the effective loss angle is reduced by $1/D$, and the effective Q is multiplied by D. For AdV suspension fibres, D∼100–200 and Q∼10^8.

Violin modes of the fibres, with fundamental near ∼500 Hz and overtones throughout the detection band, appear as narrow resonances in the sensitivity curve. Between the peaks, the $1/\omega^4$ tails of the violin modes contribute smooth thermal noise, and the overall budget between 10 and 30 Hz is dominated by the low-frequency tails of the pendulum mode.

2.3.8 Coating thermal noise

The high-reflectivity coatings on the test-mass optics are stacks of alternating SiO_2 and Ta_2O_5 layers, each a quarter laser wavelength thick. Mechanical dissipation in the tantala layers is the dominant contributor. In the frequency range of the bucket of the sensitivity curve (30–300 Hz), coating Brownian noise scales as

$$\sqrt{S_x^{\mathrm{coat}}(f)} \;\propto\; \sqrt{\frac{k_B T\,\phi_{\mathrm{coat}}\,d_{\mathrm{coat}}}{f\,w_0^2\,Y_{\mathrm{s}}}}, \tag{2.19}$$

where ϕ_{coat} is the coating loss angle, d_{coat} its thickness, w_0 the beam radius on the mirror, and Y_{s} the substrate Young's modulus. The beam radius appears squared in the denominator: larger beams average the coating deformation over a larger area and reduce the contribution.

Three active R&D directions reduce coating thermal noise:

- **Larger beams.** Advanced Virgo and Advanced LIGO run with $w_0 \simeq 6$ cm at the end mirrors; third-generation detectors target > 10 cm, limited by mirror aperture and thermal compensation.
- **Lower-loss coatings.** Amorphous silicon, titania-doped tantala, and crystalline coatings (AlGaAs) each target a smaller $\phi_{\rm coat}$.
- **Cryogenic operation.** The bracket $k_B T$ in (2.19) scales directly with temperature. KAGRA runs the sapphire test masses at ∼20 K; the Einstein Telescope low-frequency interferometer targets ∼10 K with silicon test masses.

2.3.9 Quantum noise: shot and radiation pressure

The quantum-mechanical nature of the light field produces two fundamental noises, traceable to vacuum fluctuations entering the dark port (Caves 1981). In the phase quadrature they show up as shot noise on the photodiode; in the amplitude quadrature they produce random momentum kicks on the mirrors (radiation-pressure noise).

At the output, the two contributions are

$$\sqrt{S_h^{\rm shot}(f)} \;=\; \frac{1}{L}\sqrt{\frac{\hbar c\lambda_L}{4\pi\, P_{\rm circ}}}\,\sqrt{1+(f/f_{\rm pole})^2}, \tag{2.20}$$

$$\sqrt{S_h^{\rm rp}(f)} \;=\; \frac{1}{m\,L\,(2\pi f)^2}\sqrt{\frac{16\pi\hbar\, P_{\rm circ}}{c\,\lambda_L}}. \tag{2.21}$$

Derivation.

Shot noise. Photon counting on the output photodiode gives a phase noise amplitude spectral density (2.8). Dividing by the differential phase response of an FP-Michelson (2.6) enhanced by the cavity gain gives the first line. The $\sqrt{1+(f/f_{\rm pole})^2}$ factor is the roll-off of the signal above the cavity pole; the noise is white, but referred back to strain it grows at high f.

Radiation-pressure noise. Vacuum amplitude fluctuations drive a random radiation-pressure force on each test mass. The amplitude spectral density of the force is $\sqrt{S_F} \simeq \sqrt{8\pi\hbar P_{\rm circ}/(c\lambda_L)}$, with a factor of two combining the two mirrors of a cavity. A free mass responds to a force F with displacement $F/[m(2\pi f)^2]$ at frequency f. The resulting differential displacement divided by L gives the strain noise in the second line.

Numerical check. *Advanced Virgo, design.* $L = 3$ km, $m = 42$ kg, $\lambda_L = 1064$ nm, $P_{\rm circ} \simeq 100$ kW. At $f = 100$ Hz, well below the cavity pole:

$$\sqrt{S_h^{\rm shot}} \;\simeq\; \frac{1}{3\times10^3}\sqrt{\frac{1.05\times10^{-34}\cdot 3\times10^8\cdot 1.06\times10^{-6}}{4\pi\cdot 1\times10^5}} \;\simeq\; 1.7\times10^{-24}\ \mathrm{Hz}^{-1/2}.$$

At $f = 30$ Hz, well above the pendulum but below the coating bucket:

$$\sqrt{S_h^{\rm rp}} \;\simeq\; \frac{1}{42\cdot 3\times10^3\cdot(2\pi\cdot 30)^2}\sqrt{\frac{16\pi\cdot 1.05\times10^{-34}\cdot 1\times10^5}{3\times10^8\cdot 1.06\times10^{-6}}} \;\simeq\; 3\times10^{-24}\ \mathrm{Hz}^{-1/2}.$$

Numbers of this order are consistent with advanced-detector noise budgets; verify against the current GWINC model before using in print.

Scaling with design parameters:

- Shot noise falls as $P_{\rm circ}^{-1/2}$ ⇒ high-power laser plus power recycling.
- Radiation-pressure noise grows as $P_{\rm circ}^{+1/2}$ ⇒ heavier test masses (AdV: 42 kg; aLIGO: 40 kg; ET target: 200 kg).
- Both scale with $1/L$ ⇒ longer arms help.
- Shot noise is the only noise that is reduced by increasing the laser power; radiation pressure is the price paid.

2.3.10 The Standard Quantum Limit

Shot noise and radiation-pressure noise pull the sensitivity in opposite directions as a function of $P_{\rm circ}$. At each frequency, there is an optimum power that minimises the total quantum noise. The minimum is the Standard Quantum Limit (SQL):

$$\boxed{S_h^{\rm SQL}(f) \;=\; \frac{8\hbar}{m\,L^2\,(2\pi f)^2}.} \tag{2.22}$$

The SQL is reached by saturating the uncertainty relation for the position measurement of a free mass of mass m. At the optimum power, $S_h^{\rm shot}(f) = S_h^{\rm rp}(f) = (1/2)\,S_h^{\rm SQL}(f)$.

Derivation.
Minimising $S_h^{\rm tot} = S_h^{\rm shot} + S_h^{\rm rp}$ with respect to $P_{\rm circ}$ at fixed f gives

$$P_{\rm opt}(f) \;=\; \frac{\pi\, m\, c\, \lambda_L\, (2\pi f)^2}{8}.$$

Substituting back yields (2.22). The SQL falls as $1/f$ in amplitude, which gives it the characteristic shape of a rising wall when plotted on a log-log strain plot.

The SQL is not a hard limit: squeezing and other quantum-non-demolition techniques allow the detector to beat it in a chosen frequency band. Frequency-dependent squeezing achieves this broadband, at the price of the filter cavity described in Section 2.2.5.

Numerical check. For $m = 40$ kg, $L = 3$ km, $f = 100$ Hz:

$$\sqrt{S_h^{\rm SQL}} \;\simeq\; \sqrt{\frac{8 \cdot 1.05 \times 10^{-34}}{40 \cdot (3\times 10^3)^2 \cdot (2\pi \cdot 100)^2}} \;\simeq\; 2.4 \times 10^{-24}\ {\rm Hz}^{-1/2}.$$

Advanced detectors operate close to (but not below) the SQL at a few hundred hertz, and a few dB below with squeezing.

2.3.11 Technical noises

On top of the fundamental noises listed above, every real detector carries a set of **technical noises** that depend on the details of the instrument and whose suppression is the main business of commissioning. The list below is not exhaustive:

- **Laser frequency noise.** Converts to strain through arm-length differences. Suppressed by reference cavities and by common-mode rejection of the Michelson.
- **Laser amplitude (RIN) noise.** Converts to strain through the dark-fringe offset. Suppressed by operating close to the dark port and by a dedicated intensity stabilisation loop.

- **Scattered light.** Light reflected or diffused from the nominal path, re-entering the interferometer with phase-modulated optical paths, produces non-stationary, non-Gaussian noise. Mitigated by baffles, beam dumps, and control of ambient vibrations of the scattering surfaces.

- **Magnetic noise.** Residual magnetisation of the test masses and magnetic actuators couple ambient magnetic-field fluctuations to mirror motion. Suppressed by demagnetisation, coil geometry, and active feed-forward from magnetometers.

- **Residual gas.** Fluctuations in the forward-scattered phase of the laser through residual gas molecules, plus direct momentum exchange, add displacement and phase noise. The ultra-high-vacuum system of $\sim 10^{-9}$ mbar in the arms is dimensioned on this budget.

- **Control-loop noise.** Any feedback loop that holds the instrument at the operating point injects sensor noise into the test-mass motion through the actuators. The design balances gain-at-DC (for lock) against noise-at-signal-band (to keep the control noise below the sensitivity target).

Each of these topics has a dedicated lecture in the school: seismic isolation (P. Chessa, Fri 22), coating and materials (M. Magnozzi, Fri 22), thermal compensation (I. Nardecchia, Mon 25), cryogenics (E. Majorana, Wed 27), environmental noise (R. De Rosa, Wed 27), controls (D. Bersanetti, Sat 23).

2.3.12 Reading a real sensitivity curve

A real advanced-detector noise budget (for example, the Advanced Virgo O4 budget reproduced in Bassan Chapter 13, or the publicly available GWINC model) shows the total $\sqrt{S_h(f)}$ together with the individual contributions. A checklist for reading such a plot:

1. **Identify the wall.** Below a few Hz the curve rises as a steep power law. This is the seismic and Newtonian contribution, cut off by the suspension transfer function. The foot of the wall defines the low-frequency cut-off of the detection band.

2. **Identify the bucket.** Between $\sim$50 and $\sim$200 Hz the total sits close to coating thermal noise plus, at the low-frequency side of the bucket, radiation-pressure noise. This is where most compact-binary merger SNR is accumulated.

3. **Identify the high-frequency tilt.** Above the cavity pole ($\sim$50 Hz) the shot-noise contribution rises as $\sqrt{1 + (f/f_{\rm pole})^2}$. Squeezing lowers this tilt by up to a factor of $\sim$2 in amplitude.

4. **Identify the lines.** Narrow spikes in the curve are violin modes of the suspension fibres, mechanical resonances of the suspensions, calibration lines, and electromagnetic pickup at mains frequency and its harmonics. Lines are excluded from searches for compact binary signals; they matter for continuous-wave searches.

5. **Identify the gap between total and sum-of-knowns.** Any region where the total is above the quadrature sum of the known contributions indicates an unidentified noise that the commissioning team will be working on.

The sensitivity curve is the most-used plot in the collaboration. Weekly commissioning meetings open on it; upgrade decisions are driven by it; press releases are scaled off it. Training the eye to read it is one of the goals of this block.

2.4 Network, reach, and what comes next

A single detector with a sensitivity curve at the level of Section 2.3 records strain time series in which GW events are candidates, not detections. Turning a candidate into a detection, and a detection into an astrophysical measurement, requires a *network* of detectors. This section connects strain sensitivity to astrophysical reach, sets out the role of the network, and points to the third-generation instruments discussed in depth elsewhere in the school (M. Punturo — ET, Thu 21; W.J. Weber — space-based, Thu 21).

2.4.1 From strain sensitivity to astrophysical reach

The standard figure of merit for reach is the **BNS range**: the distance at which a fiducial 1.4+1.4 $M_\odot$ binary neutron star coalescence, averaged over sky location and orientation, produces a network signal-to-noise ratio of 8 in a single detector. For a given $S_h(f)$,

$$D^2_{\rm BNS} \propto \int \mathrm{d}f \, \frac{|\tilde{h}_{\rm src}(f)|^2}{S_h(f)}. \tag{2.23}$$

The integrand is peaked in the bucket of the sensitivity curve, ∼50 to ∼200 Hz, which is why coating thermal noise and radiation-pressure noise set the range.

Typical advanced-detector ranges during O4 are: LIGO Hanford and Livingston ∼150–160 Mpc, Advanced Virgo ∼55 Mpc, KAGRA ∼10 Mpc. Detection volume scales as range cubed, so a factor-two improvement in range corresponds to a factor-eight gain in expected event rate.

Note. Range averages over source orientation and sky location. The **horizon distance** is the distance of the single best-case source (face-on, overhead) that would still produce SNR 8; it is a factor of ∼2.26 larger than the range. Both numbers circulate in the community and are occasionally confused.

2.4.2 Why a network

A single detector measures only the linear combination $h(t) = F_+ h_+ + F_\times h_\times$, weighted by the antenna-pattern functions that depend on the source direction and polarisation angle. From a single time series one cannot:

- **Localise the source** on the sky, beyond the quadrupolar antenna pattern of the detector;
- **Reconstruct the two GW polarisations** h_+ and $h_\times$ independently;
- **Distinguish a GW from a coincident noise transient** with confidence.

A network of detectors at different locations and orientations addresses all three. The quantitative statement:

1. **Two detectors** are enough for confident detection of short signals through coincidence, and for a coarse sky localisation from time-of-flight differences (an annular ring on the sky, degenerate between two antipodal directions).
2. **Three detectors** break the antipodal degeneracy and localise to an arc of a few tens of square degrees for a typical event.
3. **Four or more detectors** enable full polarisation reconstruction and sky localisation in the deg^2 regime.

The network signal-to-noise ratio combines in quadrature:

$$\mathrm{SNR}^2_{\rm net} = \sum_a \mathrm{SNR}^2_a. \tag{2.24}$$

2.4.3 Sky localisation and triangulation

The dominant information for sky localisation is the difference in arrival time at different detectors. For a pair of detectors separated by a baseline D, the GW direction-of-arrival in the plane containing the two detectors is determined by $\cos\theta = c\,\Delta t/D$. The angular resolution scales as

$$\Delta\Omega \;\propto\; \frac{1}{(\mathrm{SNR})^2\,(c\,\Delta t_{\mathrm{base}}/\lambda_{\mathrm{gw}})^2}, \tag{2.25}$$

so longer baselines and higher SNR give better localisation. Typical LIGO–Virgo baselines are ∼10 ms (LL–LH ≃ 10 ms, LL–V ≃ 27 ms, LH–V ≃ 27 ms); adding KAGRA and LIGO-India brings the longest baseline above 40 ms, with corresponding gains in localisation.

The scientific impact is concrete: GW170817 was localised by LIGO–Virgo to ∼28 deg^2, small enough for optical follow-up telescopes to find the kilonova in less than 11 hours. This level of localisation, together with the low event rate and short electromagnetic counterpart lifetime, is what closes the loop with multi-messenger astronomy.

2.4.4 The global network today and in the near future

The current second-generation network:

- **LIGO Hanford** (USA, Washington), $L = 4$ km, operating.
- **LIGO Livingston** (USA, Louisiana), $L = 4$ km, operating.
- **Virgo** (Italy, Cascina), $L = 3$ km, operating.
- **KAGRA** (Japan, Kamioka), $L = 3$ km, underground, cryogenic, operating.
- **LIGO-India** (Aundha, Maharashtra), $L = 4$ km, under construction, with first observations expected in the first half of next decade.

A five-detector network at LIGO-Hanford, LIGO-Livingston, Virgo, KAGRA, and LIGO-India is expected to produce localisations below 10 deg^2 for a substantial fraction of detected events, with duty cycles allowing near-continuous network coverage.

2.4.5 Third-generation detectors

Two third-generation detectors are in advanced design:

- **Einstein Telescope** (Europe, site decision expected in 2027-2028). Triangular topology with three co-located instruments, each with $L = 10$ km underground arms, and a **xylophone** split into a low-frequency, cryogenic, low-power interferometer and a high-frequency, room-temperature, high-power interferometer. An alternative L-shaped topology with $L = 10$ km is also being proposed. Sensitivity target one order of magnitude better than Advanced Virgo, with low-frequency reach down to ∼3 Hz.
- **Cosmic Explorer** (USA). L-shaped with $L = 40$ km arms above ground, scaled from the Advanced LIGO design. Target sensitivity similar to Einstein Telescope in the mid-band, with even better high-frequency reach.

The physics case covers cosmology with standard sirens, neutron-star equation of state, stochastic backgrounds, and primordial-black-hole searches at cosmological distances. M. Punturo's lecture (Thu 21, 14:30) covers the ET site, design, and science case in detail; W.J. Weber (Thu 21, 16:35) covers the space-based sensitivity and design.

2.4.6 Bridge to the rest of the school

The material of Block 2 is an overview. Each of the subjects touched on here is covered in a dedicated lecture later in the school:

- Optical configurations: Fabry–Perot, dual recycling, signal extraction, output mode cleaner — **A. Perreca** (Fri 22 & Sat 23).
- Length and alignment sensing and control, lock acquisition, hierarchical control — **D. Bersanetti** (Sat 23).
- Quantum noise, squeezing, filter cavities, quantum-non-demolition techniques — **F. Sorrentino** (Tue 26).
- Suspension design, seismic isolation platforms, payload engineering — **P. Chessa** (Fri 22).
- Coating and substrate materials, cryogenic optics — **M. Magnozzi** (Fri 22); cryogenics: **E. Majorana** (Wed 27).
- Input and output optics, laser stabilisation — **M. Galimberti** (Mon 25); scattered-light mitigation — **L. Conti** (Mon 25 & Tue 26).
- Thermal compensation — **I. Nardecchia** (Mon 25).
- Environmental noise and its impact on the detector — **R. De Rosa** (Wed 27).
- Data analysis: matched filtering, parameter estimation, unmodelled searches, stochastic backgrounds — **F. Pannarale** (Tue 26 & Wed 27); space-based data analysis: **R. Buscicchio** (Tue 26).
- Third-generation detectors: Einstein Telescope and Cosmic Explorer — **M. Punturo** (Thu 21); space-based sensitivity — **W.J. Weber** (Thu 21), **G. Wanner** (Fri 22), **L. Sala** (Mon 25).
- Scientific achievements of current detectors — **B. Patricelli** (Wed 27).

The compact formulas of this block are the back-of-the-envelope tools to cross-check everything that follows.

Block 2 — Summary

- **Michelson topology.** Differential arm-length readout on a dark fringe is the optical skeleton of every ground-based detector. Shot noise on a bare Michelson with reasonable laser power sits at $\sim 10^{-20}$ Hz$^{-1/2}$, two to three orders of magnitude above the target.
- **Fabry–Perot + recycling + squeezing.** FP arm cavities increase the phase response; power recycling increases the circulating power; signal recycling reshapes the frequency response; squeezing lowers the vacuum contribution to the readout.
- **Noise budget.** Three regions map onto three physics drivers: seismic and Newtonian at low frequency, thermal in the bucket, quantum at high frequency. The sensitivity curve is the designer's map.
- **Standard Quantum Limit.** The competition between shot noise and radiation-pressure noise sets an envelope, $S_h^{\mathrm{SQL}} = 8\hbar/(mL^2(2\pi f)^2)$. Advanced detectors operate close to the SQL in the bucket; squeezing beats it.
- **Network.** Strain sensitivity becomes astrophysical reach through the BNS range. Sky localisation and polarisation reconstruction require three or more detectors; the global network is the only way to do GW astronomy in practice.

Take-away. A GW detector is a multi-km precision optical machine in which every noise source has been pushed to the limit allowed by known physics. No single technique dominates; the instrument works because all of them have been driven to their own frontiers simultaneously.

Block 2 — Key equations

1. GW-induced phase shift (FP Michelson, below cavity pole):

$$\Delta\varphi_{\rm gw} \;=\; \frac{4\pi L}{\lambda_L}\,h \;\cdot\; \frac{2\mathcal{F}}{\pi}.$$

2. Shot-noise-limited strain (simple Michelson):

$$\sqrt{S_h^{\rm shot}(f)} \;=\; \frac{1}{L}\sqrt{\frac{\hbar c\lambda_L}{4\pi P_{\rm in}}}.$$

3. Fabry–Perot cavity pole and effective arm length:

$$f_{\rm pole} \;=\; \frac{c}{4\,\mathcal{F}\,L}, \qquad L_{\rm eff} \;=\; \frac{2\mathcal{F}}{\pi}\,L.$$

4. Thermal-noise spectrum of a damped oscillator (FDT, viscous damping):

$$S_x(\omega) \;=\; \frac{4k_B T\,\omega_0/Q}{m\left[(\omega^2-\omega_0^2)^2+(\omega\,\omega_0/Q)^2\right]}.$$

5. Pendulum isolation transfer function (above resonance):

$$\left|\frac{x_{\rm mass}}{x_{\rm ground}}\right| \;\simeq\; \left(\frac{f_0}{f}\right)^2.$$

6. Standard Quantum Limit:

$$S_h^{\rm SQL}(f) \;=\; \frac{8\hbar}{m\,L^2\,(2\pi f)^2}.$$

7. BNS range scaling:

$$D_{\rm BNS}^2 \;\propto\; \int \mathrm{d}f\,\frac{|\tilde{h}_{\rm src}(f)|^2}{S_h(f)}.$$

Order-of-magnitude anchor. Simple Michelson with $L = 3$ km and $P_{\rm in} = 10$ W: $\sqrt{S_h^{\rm shot}}\sim 10^{-20}$ Hz$^{-1/2}$. Advanced detector: $\sqrt{S_h}\sim 10^{-23}$ Hz$^{-1/2}$ at 100 Hz.

Block 2 — Further reading

[1] Massimo Bassan, ed. *Advanced Interferometers and the Search for Gravitational Waves*. Vol. 404. Astrophysics and Space Science Library. Cham: Springer, 2014. ISBN: 978-3-319-03791-2. DOI: 10.1007/978-3-319-03823-0.

[2] Michele Maggiore. *Gravitational Waves. Vol. 1: Theory and Experiments*. Oxford: Oxford University Press, 2007. ISBN: 978-0-19-857074-5. DOI: 10.1093/acprof:oso/9780198570745.001.0001.

[3] Peter R. Saulson. *Fundamentals of Interferometric Gravitational Wave Detectors*. 2nd ed. Singapore: World Scientific, 2017. ISBN: 978-981-314-307-4. DOI: 10.1142/9book.

[4] J. Aasi et al. "Advanced LIGO". In: *Classical and Quantum Gravity* 32.7 (2015), p. 074001. DOI: 10.1088/0264-9381/32/7/074001. arXiv: 1411.4547.

[5] F. Acernese et al. "Advanced Virgo: a second-generation interferometric gravitational wave detector". In: *Classical and Quantum Gravity* 32.2 (2015), p. 024001. DOI: 10.1088/0264-9381/32/2/024001. arXiv: 1408.3978.

[6] T. Akutsu et al. "Overview of KAGRA: Detector design and construction history". In: *Progress of Theoretical and Experimental Physics* 2021.5 (2021), 05A101. DOI: 10.1093/ptep/ptaa125. arXiv: 2005.05574.

[7] Adrian Abac et al. "The Science of the Einstein Telescope". In: *arXiv e-prints* (2025). arXiv: 2503.12263 [gr-qc].

Block 2 — Exercises

1. **Michelson output with an arm-length offset.** Consider a simple Michelson with arms of unequal static length, $L_x = L + \delta$ and $L_y = L - \delta$, with δ a small offset chosen to park the instrument slightly off the dark fringe. Expand the output power (2.5) to first order in both δ and in a GW-induced length change, and derive the photocurrent as a function of $h(t)$. Show that the DC readout signal is linear in h and proportional to δ. Estimate the optimal δ that balances laser-intensity coupling against shot-noise coupling, for $P_{\rm in} = 10$ W and a target RIN level of 10^{-8} Hz$^{-1/2}$ at the detection photodiode.

2. **Fabry–Perot cavity pole and finesse.** A symmetric FP cavity has input and end mirrors with amplitude reflectivities r_1 and r_2. Starting from the standard round-trip amplitude relation $E_{\rm circ} = t_1\, E_{\rm in} + r_1 r_2\, \mathrm{e}^{2ik_L L}\, E_{\rm circ}$, derive the finesse $\mathcal{F} = \pi\sqrt{r_1 r_2}/(1 - r_1 r_2)$ and the cavity pole (2.11). For an Advanced Virgo arm cavity with $r_1^2 = 0.986$ (ITM power reflectivity) and $r_2 = 0.99999$ (ETM, taken as perfect for this exercise), compute $\mathcal{F}$ and $f_{\rm pole}$ numerically and compare with the published values.

3. **Pendulum thermal noise with viscous vs structural damping.** The FDT result (2.17) assumes *viscous* damping, γ constant. Real suspensions in cryogenic or monolithic configurations are better modelled by *structural* damping, for which the loss angle ϕ replaces $\gamma/(m\omega)$. Starting from the FDT (2.16) with $\alpha(\omega) = 1/[\kappa(1+i\phi) - m\omega^2]$, derive the low-frequency behaviour $S_x(\omega) \propto 1/(\omega\phi\, m\omega_0^2)$ and compare the dimensional structure with the viscous case. Explain why structural damping gives a more favourable low-frequency thermal-noise spectrum when $\phi \ll 1$ is nearly frequency-independent. Cite the relevant chapter of Saulson as reference.

4. **Optimal laser power at the SQL.** Starting from the shot-noise (2.20) and radiation-pressure (2.21) spectra, compute the optimal circulating power $P_{\rm opt}(f)$ that minimises their sum, and show that $S_h^{\rm shot}(f) + S_h^{\rm rp}(f)|_{P_{\rm opt}} = S_h^{\rm SQL}(f)$. For $m = 40$ kg, $L = 4$ km, and $f = 100$ Hz, give a numerical estimate of $P_{\rm opt}$ and compare with the actual circulating power in Advanced LIGO. Discuss the implications for the optimisation with a frequency-dependent squeezing system.

5. **Triangulation from timing.** Two detectors at locations $\vec{r}_1$ and $\vec{r}_2$ on the Earth's surface record a signal with time offset $\Delta t = t_2 - t_1$, measured with uncertainty $\sigma_{\Delta t}$. Show that the source direction is constrained to a circle on the sky, and that the opening angle of the circle is determined by $\cos\theta = c\,\Delta t/|\vec{r}_2 - \vec{r}_1|$. For the LIGO-Hanford / LIGO-Livingston baseline ($|\vec{r}_2 - \vec{r}_1| \simeq 3000$ km) and an SNR of 10 on a BNS signal with $\sigma_{\Delta t} \sim 1/(2\pi f_{\rm peak} \cdot \mathrm{SNR}) \sim 1$ ms,

estimate the width of the triangulation ring. Compare with the typical LIGO–Virgo–KAGRA localisation area during O4 and explain the role of the third detector in breaking the degeneracy.